Neural Dynamics based on EEG and diffusion MRI: Potential in studying stroke

Pablo Maceira Elvira

A thesis presented for the degree of
Master of Science in Biomedical Engineering

Evaluation committee:

- University Professor: Prof.Dr. Frans C.T. van der Helm
- Supervisors:
  - Dr. Yuan Yang
  - MSc. Lena Filatova
- External Reviewer: Dr.Eng. Sander Wahls

3mE- Mechanical, Maritime and Materials Engineering
TU Delft
The Netherlands
June 12th of 2017

Contents

Dedication

A mi Papá, a quien más admiro, por enseñarme, inspirarme, motivarme y acompañarme todos los días; todo lo que he hecho y lo que soy, te lo debo a ti. A mi Mamá, en quien pienso y a quien extraño todos los días; no podría estar más agradecido y feliz de ser tu hijo. A mi otra Mamá, ejemplo de cariño y entrega, que me ha traído tanta dicha. A Álvaro, Mercedes y Eugenio, que son lo mejor que me ha pasado en la vida. A mis amigos queridos, miembros honorarios de mi familia, por acompañarme también; ustedes saben quiénes son. A Dios, por brindarme esta vida tan maravillosa.

To all the true friends I've made over the past years, all of you who have become an anchor and a family far from home and have helped me keep my sanity (more or less).

Abstract

After stroke, functional recovery may be promoted during the first six months through rehabilitation. Several events are thought to lead to regaining lost functions, among which the remapping of affected limbs to other regions of the cortex is a frequent occurrence. High spatial resolution brain imaging techniques, like magnetic resonance imaging (MRI), may be used to observe the affected areas and assess the severity of the lesions, but are unable to provide much insight on dynamic changes in brain function. An alternative non-invasive technique possessing an excellent temporal resolution to observe transient events is electroencephalography (EEG), a method limited by a low spatial resolution. This study aims to combine 62-channel EEG recordings with anatomical information derived from structural MRI and diffusion-weighted imaging (DWI) to improve the low resolution of EEG. During EEG acquisition, stroke patients (N = 3) and age-matched healthy controls (N = 2) received electrical impulses at both index fingers, stimulating both brain hemispheres sequentially through somatosensory feedback. After a static estimation of the current time series of candidate sources distributed over the brain cortex, a multivariate autoregressive (MAR) model was used to estimate the causal interactions between those found to be active due to the applied stimulus. The result was a visualization of the information transfer between active sources. A reasonably accurate estimation was achieved, even in presence of low signal to noise ratio (SNR) of EEG. Physiologically plausible source locations and connecting pathways were found, but an explanation of the observed phenomena and the interpretation of the differences between patients and controls is beyond the scope of this thesis, as a more extensive study is needed for this purpose. Consistent results found within subjects provide evidence of the potential value of this method in longitudinal studies, even when a comparison between subjects were not possible due to confounding factors (i.e. SNR differences). The obtained results support the candidacy of this method in the study of stroke, as it was found to be useful to track the information flow in the brain and might constitute a first step towards the development of a precise prognostic model of stroke.

List of variables

A: Matrix of weighting coefficients in a MAR model

A_l: Weighting matrix in VBMEG MAR model, initialized based on estimated anatomical connections

A_L^{-1}: Variance matrix of Z

α_{0n}^{-1}: Current variance (inverse precision)

$\bar{\alpha}_{0n}^{-1}$: Mean current variance

b: Magnetic field

b_∞: Primary field

β^{-1}: Average noise variance, estimated from the baseline

C_n: Index for anatomically connected sources to the nth source

C_{uu} = Autocovariance of the baseline

D: Smooth currents (dipole space)

δ: Time delays in signal propagation along white matter tracts

e_n: Noise for a single time series in a MAR model

E_n: Noise matrix for the full MAR model

E: Electric field

η: Measurement noise

f_s: Number of fibers sprouting from the seed ROI in the currently considered pair

f_t: Number of fibers estimated between a pair of ROIs

ϕ_s: Potential basis function (BEM)

g: Leadfield vector

G: Leadfield matrix

$\hat{G}$: Smooth Leadfield matrix

$\gamma_{0n\alpha}$: Hyperparameter controlling the shape of the gamma function describing the posterior distribution of the currents' variance

I_p: An identity matrix matching the size of the number of dipoles p

j: Current density (Biot-Savart)

j^p: Primary currents

j^v: Passive currents

K,k: Solution kernels reflecting the structure of the cortical model for solving the forward problem. Generalized expression for the Leadfield matrix

k_∞: Infinite homogeneous model for solving the forward problem

$L(D)$: Energy function associated to the prior distribution of the currents D

λ: Regularization parameter for solving an L_2 norm minimization problem

M = Measurements (EEG or MEG)

μ_0: Permittivity of empty space

N = Number of sensors (electrodes)

ν: Parameter controlling the relative weight between the reconstruction error and the regularization term in a least squares problem

P: Number of dipoles

Θ: Dipole orientation

q = Dipole moment (orientation and magnitude)

r: Observation point (sensor coordinates)

r': Source point (dipole coordinates)

S: Number of surfaces in tessellation

σ: Medium conductivity

σ_0: Unit conductivity of an infinite homogeneous medium

Σ_0: A regularization matrix

Σ_α^{-1}: Current covariance matrix, with the precision (inverse variance) along its diagonal

Σ_C: Diagonal matrix with the Trace of the Autocovariance matrix C_{uu} repeated along its diagonal

Σ_G^{-1}: Noise covariance matrix

T: Time

$U1(D)$: Energy function associated to the probability of the measurements given the currents

v: electric potential

v_∞: Primary potential

v_s: Number of voxels in seed ROI

v_t: Number of voxels in target ROI

W: 3-dimensional weighting matrix in a MAR model

W_L: Gaussian smoothing filter for smoothness constraint

x_n: Vector containing a number of time samples previous to y_n

y_n: nth sample of a time series in a MAR model

Z = Coarse currents (source space)

ψ_s: Weighting basis function (BEM)

ω: Reconstruction error in a MAR model

Chapter 1

Introduction

1.1 Stroke: The Ailment and its Impact

Stroke is caused, in general terms, by the interruption of blood supply (oxygen) to specific areas of the brain [1], and it refers to the clinical condition of rapidly developing neurological deficit in the affected areas (when not due to seizure activity) [2]. Stroke caused by a deprivation of blood supply from flow blockage is called ischemic stroke, and may have different origins, thrombosis or an embolus within a blood vessel being the most common. Other events that may result in such an oxygen deficit may be occlusion caused by a hematoma or tumor or inflammation of the arteries, but these cases are rare [2]. Stroke may also occur as a result of the rupture of a blood vessel (hemorrhagic stroke) [3]. There are several symptoms that may arise as soon as an occlusion occurs (numbness or weakness of the face or limbs, normally on one side of the body [1]) and quickly reacting to them greatly improves the chances of survival and recovery for patients.

Stroke is the third most common cause of death in industrialized countries, only surpassed by heart disease and cancer [4]. In Europe, as the proportion of elderly members of the population grows on a yearly basis, and the likelihood of having a stroke doubles every 10 years after the age of 55 [5], stroke incidents are expected to increase from 20% of the 65+ population, observed in the year 2000, to 35% by 2050, which would result in a decrease in the European population from 728 million in 2000 to 705 million inhabitants in 2050 [6]. For this reason, preventing cerebrovascular accidents resulting in stroke and properly reacting to such episodes when they occur has become a major concern for all parties involved.

Stroke survivors tend to suffer from a variety of impairments that become evident during the first 6 months after the occurrence of the cerebrovascular accident, being hemiparesis, cognitive deficits and depressive symptoms some of the most common ones [7]. The severity of their impairment depends on the location and spread of the damaged region in the brain. Consequently, patients having suffered from stroke face a dramatic decrease in their quality of life.

According to the World Health Organization (WHO), 15 million people suffer a stroke every year around the world, from which 5 million are left permanently disabled [8]. The global prevalence of stroke was estimated to be 33 million in 2015 [9]. This results in a large number of productive years lost by those patients (Disability adjusted life years-

DALYs), that was of 38 million DALYs in 1990 and that is expected to be of 61 million DALYs in 2020, placing a huge burden on the global population, as healthy, productive people need to support an ever enlarging non-productive population [8]. Even though major risk factors such as high blood pressure and smoking have been gradually controlled and reduced worldwide, the generalized aging of the population observed in most countries has led to the expected incidence of stroke for the following years to elevate [8].

The increasing number of stroke patients results in a large expenditure in healthcare. For example, in 2003, the Netherlands spent an average of € 16,000 per patient during the 6 months following the accident in medical costs [10]. According to the Dutch National Institute for Public Health and the Environment (RIVM), in the 2002 report on Dutch Health Status and Forecasts [11], a total amount of 417 million Euros were spent on care given to stroke patients in 1999, an amount that according to Struijs et al. [12] remained relatively constant (at least until 2005, when their work was published), albeit a slight increase. The enlargement of the population of aged individuals observed during the last 10 years, alongside the development of more effective treatment, has caused these numbers to augment. The aforementioned report by the RIVM stated that the costs related to stroke in the Netherlands, which constituted about 3% of the costs in Healthcare in that country in 2002, where expected to increase 1.5% every year [11].

Additionally, there are many sources of expenditure that are not so obvious, such as social services and caring costs [13]. More than 50% of stroke survivors return to their home after being released from the hospital and are cared for by informal care givers, such as their families [14]. Van Eeden et al. [14] strived to perform a more comprehensive analysis of the costs, as they included the intervention costs (those that contribute to the development and administration of the Self-Management Intervention and the augmented cognitive behavioral therapy), the health-care sector costs (general practitioner (GP) visits, hospital visits, and medication), patient and family costs (travel costs, costs of informal care, productivity losses and home adjustments) and costs outside the healthcare sector (productivity costs). Such broader studies offer a more accurate image of the costs related to stroke and accentuate the relevance of improving the rehabilitation therapies provided nowadays. 3 years later, Van Eeden et al. [15] reported that the total societal costs in the Netherlands, for 1 year post-stroke patients were € 29,484, from which 74% was spent over the first 6 months. This amounts to € 21,818.16, which approaches quite well the estimation the RIVM offered back in 2002 [11].

1.2 Treatment

When stroke occurs, an immediate and efficient response from healthcare providers is paramount, so that the patient may achieve the best possible recovery, as a full recovery is typically not accomplished [16]. Nevertheless, treatment applied to stroke survivors has proven to have variate, unpredictable results [17], which has so far hindered the overall rehabilitation process. Nelles et al. [18] found that passive movements induced on patients having suffered from stroke generates some of the activation patterns of those observed when the same movement is performed actively after substantial motor recovery has been achieved. This phenomenon has been used to promote re-learning by striving to trigger the neuroplastic mechanisms that seem to underlie the brain's resilience and capacity to reconfigure itself [19]. The problem is, though, that this neuroplastic mechanism is not yet fully understood, which makes it challenging for physicians to determine a rehabilitation therapy that might effectively trigger structural changes in the brain that would, in turn, allow for a patient to recover lost functionality.

Langhorne et al. [20] carried out a review of the literature in order to lay down a map of relevant rehabilitation interventions and they found that some forms of rehabilitation therapies do seem to have a positive effect in either the recovery or the compensation (depending on the characteristics and particularities of every patient) of lost functions, while for others evidence of actual benefits could not be found. Naturally, variables such as the quality of the therapy itself also play a role in the degree and rate of improvement in patients, but subtle differences in the lesions present in each case may hinder the process, regardless of the thoroughness and quality of the therapy provided, which calls for training to be adapted, tailor-made even, to every single case.

1.3 Neuroplasticity

Brain plasticity or neuroplasticity refers to the ability of the brain to remodel neuronal cortical connections, triggered by a goal-oriented experience (learning) [21]. This mechanism is not yet entirely understood, but several hypothesis exist behind its functioning, such as long-term potentiation (improvement of the execution of a task through repetition; "persistent increase in synaptic strength following high-frequency stimulation of a chemical synapse" [22]) and long-term depression ("activity-dependent reduction in the efficacy of neuronal synapses lasting hours or longer following a long patterned stimulus" [23]). Synaptic plasticity in cortical horizontal connections is also thought to be behind the reorganization of the cortical map [24]. The occurrence of this reorganization has been reported to vary and may depend on the underlying mechanism causing that specific reorganization in an individual [24]. Therefore, even though there seems to be enough evidence of neuroplasticity in stroke patients, an optimal way of triggering it and of achieving a specific desired reorganization in the maps of the brain is yet to be found. Better understanding neuroplasticity by knowing which stimuli reconfigure brain maps in a certain way may hold in itself the key to optimizing rehabilitation therapies so as to achieve a functional recovery through neural compensation.

Neuroplasticity has been attributed to multiple underlying events, such as connective redundancy, axonal sprouting resulting in the formation of new synapses, functional take-over by the contra-lateral homologous cortex, etc. [25]. Training and other forms of rehabilitation have been found to promote changes in the representation of affected limbs on the cortex, relocating them to healthy regions of a patient's brain. Frequently, repurposed areas may be found in the peripheral areas of infarction, the homologous contra-lateral region and adjacent supplementary motor areas (SMA) [25]. Phenomena such as axonal sprouting does not normally occur in adult individuals (they typically occur during maturation), but the occurrence of injuries enables these mechanisms to be triggered once again, approximately during the first 6 months after injury [25], which is why therapy provided within this time frame yields the best results. This remapping of limbs in the cortex alters the functional connectome, which most likely results in topological changes in the brain network [26].

1.4 The Human Connectome

The Human Connectome is a comprehensive structural description of the elements of a human brain network and the elements connecting them to each other [27]. This description may be performed at different scales, going from the microscale (single neurons and their synapses), through the mesoscale (components within regions), to the macroscale (brain regions and the pathways leading to them). An alternative meaning for the term "connectome" is that referring to the sequence of co-activated areas (i.e. functional connectivity) [28], which is the one used in the present paper.

1.5 An Effort to Understand Neuroplasticity

The problem of understanding the way in which the brain reconfigures itself may be approached in different ways. One of the main strategies adopted to this end consists of studying the way in which the brain responds to external stimuli. Hypothetically, acquiring some notion about the effects a particular form of stimulus has on the rearranging of the brain network could, in principle, make it possible for a specific, desired configuration to be induced on the brain. Several techniques exist to measure and observe brain activity, but all of them have technical aspects that obscure the observed phenomena. For example, techniques like functional magnetic resonance imaging (fMRI) posses a high spatial resolution, providing accurate information on the exact location of active areas within the brain, but have a poor temporal resolution that results in the loss of information on transient events. On the other hand, electroencephalography (EEG) has a high-enough temporal resolution to measure transient responses, but a low spatial resolution, providing only a general idea of where the active areas are located [29].

To face this problem, a conglomerate of methods has been developed in an attempt to combine the advantages of multiple brain imaging techniques to compensate for their individual weaknesses. In general, these methods seek to combine brain activity measurements performed while applying a known perturbation with mathematical constraints derived from prior knowledge of physiological phenomena, in order to determine which areas of the brain are activated as a response to such stimuli. However, this activation is rarely isolated and seldom exclusive to a given episode, which makes it difficult to be attributed to a specific event.

Multiple techniques for brain source localization have emerged from the collective work of many research groups worldwide, being gradually refined so that an ever more accurate identification of participating components of the brain can be performed. In general, this process consists of two stages, known as the **Forward Problem** and the **Inverse Problem**.

The solution of the *Forward Problem* requires building a model of the brain to be studied alongside its surrounding tissues (i.e. skull, scalp, etc.) with their respective geometric and physical characteristics (i.e. conductivity), including a conglomerate of prospective sources of neural activity so that a corresponding primary magnetic field or primary scalp potential at each of these sources can be calculated relative to the location of the observation points (i.e. electrodes) [30]. To do this, several assumptions can be made (i.e. consider the skull to be spherical) [29], trying to find an equilibrium between model accuracy and computational complexity.

Once the model of the brain has been built and its corresponding magnetic field or scalp potential has been calculated, depending on whether magnetoencephalography (MEG) or EEG recording techniques are involved, the *Inverse Problem* can be solved. Previously obtained measurements of brain activity are used as input in order to estimate the location of neural activity related to a given, known stimulus. These locations are determined by estimating the magnitude of the currents and (usually) defining a threshold above which those currents will be assumed to be related to the stimulus. This problem is inherently complicated, as it is severely underdetermined; far more sources exist than sensors to measure their activity.

Consequently, the ideal case would be for a method to be implemented such that it was possible to benefit from the advantages of every technique while avoiding their corresponding disadvantages, so as to effectively observe the effects external stimuli have on the activation patterns of the brain. Nevertheless, the estimation of the location of active sources in the brain of stroke patients constitutes but a fraction of the information needed to understand the effects the applied rehabilitation has on their recovery. Acquiring a full perspective of the structural changes undergone in a patient's brain during and after rehabilitation requires not only to know where information is processed, but also the regions between which this information is transferred. In other words, it is of utter importance to understand the way in which the brain network is modified in response to the therapy so that it might be possible to alter it in a specific way. A first approach at understanding these changes might be to compare the conventional information flow between interconnected brain areas found in healthy subjects with those displayed by patients, so that differences in functional connectivity may be observed.

The presently described research effort has studied the gradual "evolution" of multiple brain source localization methods, as well as different possibilities for building a dynamic model describing source interactions. This search on the state of the art has made it possible to select what seems like an appropriate candidate for the intents and purposes of this endeavor. A physiologically constrained Bayesian estimation algorithm is used to locate active brain sources. These sources, combined with white matter tracks estimated from DWI, are used to build a multivariate autoregressive (MAR) model to describe the causal interactions between regions of interest (ROIs).

This method, called Variational Bayesian Multimodal Encephalography (VBMEG) has been developed by the Japanese company ATR (Advanced Telecommunications Research Institute International). It has been found to yield accurate localization results when processing data related to a face recognition task [31], but its localization potential for processing different forms of stimulation remains unexplored.

1.6 Problem Definition and Goal

The underdetermined nature of the inverse problem calls for structural, physiological and functional information to be combined to find the location of active areas in the brain related to a specific form of stimulus. Among the methods published over the past years, the VBMEG method has shown potential both in locating these active sources and estimating the pathways connecting each of these to others. This dynamic model of activity between brain sources is useful in providing some notion of activation causality and information transfer. Nevertheless, the accuracy of this method remains to be explored when using more complex forms of stimulation (i.e. somatosensory perturbations). Furthermore, published results have focused on healthy subjects exclusively, leaving the matter of its potential to study patients untested.

Therefore, the present work will investigate the dynamic interactions between sources activated by an external somatosensory stimulus, comparing those found in healthy subjects with those found in stroke patients. To this end, a multimodal brain imaging method combining anatomical data from structural and diffusion MRI with functional information from EEG will be applied to estimate the location of active brain sources. A Multivariate Autoregressive (MAR) model will then be used to estimate the activation causality of the sources, providing some notion of the pathways used by active sources to relay information to one another. This research effort is meant to serve as a proof of concept for the potential of the VBMEG method in future studies of the topological changes in the brain of stroke patients.

1.7 Layout of this Thesis

Chapter 2 of the present document offers an overview of the solution of the brain source localization problem, with special emphasis in the techniques applied by the currently used method, as well as a general explanation of the MAR model. **Chapter 3** presents a description of the whole process carried out to estimate the current densities of each source and the causal interaction among them. **Chapter 4** presents the obtained results, later to be discussed in **Chapter 5**, where possibilities for further improvement in future studies are also contemplated. **Chapter 6** portraits the conclusions of this work and the **Appendix A** offers more exhaustive, mainly mathematical descriptions of the concepts employed in the VBMEG method. Finally, **Appendix B** offers an explanation of the aspects considered when discriminating independent EEG components during its preprocessing.

Chapter 2

Theoretical Background

The multimodal brain imaging method used in the present work is a combination of probabilistic (Bayesian) methods with a Multivariate Autoregressive (MAR) model, which is capable of estimating active sources over a period of time, as well as the causality between their activation. This chapter will offer an explanation of the process of "Brain Source Localization", as well as the particularities of the applied methods.

As it was briefly mentioned in the introduction, the problem enclosed in source localization has its origin in the fact of having unfit instruments to measure the contributions of each region of interest (ROI) in the brain. The recorded activity acquired using imaging techniques such as EEG and MEG can be attributed to pyramidal neurons in the brain, which have a perpendicular orientation with respect to its cortex. The resulting scalp potential or magnetic field can be measured using the aforementioned techniques, but the number of ROIs far exceeds the number of sensors that can be used to perform the measurements, which is why, mathematically, this problem is underdetermined.

To face these issues, a number of methods have been developed to narrow down and pinpoint the location of sources portraying an activity pattern that might be related to a specific episode or event (i.e. external stimulus). These techniques may avail themselves of extra information derived from structural (MRI/DWI) and functional (fMRI) recordings to further constrain and reduce the set of candidate sources. In general, the whole process may be broken down into several steps, which are described next.

2.1 Construction of the head model

The first step consists of building a mathematical model of the head that will contain the candidate sources to be related to the measurement of the scalp potential or the magnetic field. This model can be built in different ways and can have an array of complexities, carrying along a corresponding variety of difficulties and computational costs to solve. The simplest models may be defined as a single sphere or series of concentric spheres with candidate sources placed on the surface. While such a model may be solved with relative ease, the accuracy of the obtained results may not be sufficient, its resemblance to an actual human head being so poor. On the other hand, building a head model mimicking the geometric and physical properties of a human head may prove too difficult to solve, which is why an adequate balance between computational complexity and model fidelity must be found.

Crouzeix et al. [32] compared single- and multi-layered spherical and realistic models, and found that a good option offering an acceptable degree of fidelity, while remaining relatively easy to compute is the concentric shell head model. This model is comprised of concentric layers, corresponding to multiple tissues of the head (brain, cerebro-spinal fluid, skull, scalp, etc.), possessing geometries and physical properties (i.e. conductivity) similar to those found in a real head. Some assumptions can be made to simplify the calculations, such as the conductivity found in each shell being isotropic. Each of these shells may be modeled using a general atlas of the anatomy of the human head, but better results are obtained when these geometries are derived from anatomical information specific to each individual, as even small inter-subject differences may lead to inaccuracies in the estimation [33]. Once the layers corresponding to these tissues have been defined, a set of candidate sources must be incorporated into the brain layer. There are different possibilities, but a common practice in recent projects has been to divide the cortex into parcels, normally triangular, and assign candidate sources to either the vertices of these elements or to place them at the geometric center of each triangle [34].

It is pertinent now to mention that difficulties may arise when tessellating the cortex of stroke patients presenting large lesions, as the inhomogeneity of the surface of the cortex may make it impossible to lay down a homogeneous mesh; this may have serious computational implications. The way in which candidate sources are defined in the brain plays a major role in the accuracy of the estimation of their current densities, but also on the computational costs involved. Setting up a homogeneous mesh on the cortex, as mentioned recently, allows for an efficient numerical method, called Boundary Element Method (BEM) to be used. In general, this method consists of approximating the solution to a partial differential equation (PDE) by calculating the solution to the PDE at the boundary of the domain and then using this information to find the solution inside the domain [35]. In terms of the problem at hand, this is convenient as it allows to place a mesh exclusively on the surface of the brain, which makes it much lighter to compute. Nevertheless, when setting up such a mesh is not possible, some alternatives exist.

One of them utilizes a Finite Element Method (FEM) instead, which allows to use inhomogeneous elements capable of fitting any geometry, but has the disadvantage of having to mesh the whole volume (of the brain, in this case) which dramatically elevates the computational costs involved. Other alternatives, such as using the contra-lateral region to mirror the damaged area, have been explored [33], but subtle differences between both hemispheres still lead to inaccuracies in the estimation. For this study, though, stroke patients with relatively small lesions were selected in order to avoid major problems in setting up the mesh.

Once the location of the candidate sources has been defined, the remaining parameters to be estimated are the source orientation and the source magnitude, which together constitute the moment of the dipoles. Whenever anatomical information from MRI data is available, it is possible to differentiate between white and gray matter inside the brain, which can be used to fix the orientation of the sources. This can be done because, as mentioned before, the currents result from the activity of pyramidal neurons, which are perpendicular to the cortex. In practice, the T1 MRI scan is segmented into white and gray matter, a boundary surface is set at the gray matter and all sources are set to reside on it, with a perpendicular orientation to this surface. Therefore, the only unknown parameters left are the source's current magnitudes.

2.2 Solving the Forward Problem: Calculating the Leadfield

Once the head model has been built, the next step consists of finding the magnetic field (when MEG measurements are involved) or the scalp potential (when using EEG data) related to a specific source distribution as perceived by a specific sensor layout, which constitutes the solution of the *Forward Problem.* As the present work used EEG measurements only, MEG-related descriptions will not be included here. The relationship between the electric field and the current densities, leading to the calculation of the primary potential, may be found in *Appendix A*. The primary potential is the electric potential observed at a certain sensor location r due to the primary current exclusively. The expressions for this quantity (also shown in *Appendix A*) constitutes the boundary integral equation for solving the forward problem for scalp potentials (EEG).

The solution to the boundary equation previously mentioned may be factored and expressed as the product of a field kernel and the dipole moment [34], and the form this kernel takes depends on the type of model chosen. The solution may be enunciated as:

$$v(\mathbf{r}) = \mathbf{k}^T(\mathbf{r}, \mathbf{r'}) \cdot \mathbf{q} \tag{2.1}$$

With $\mathbf{k}(\mathbf{r}, \mathbf{r'})$ being a 3x1 vector kernel function of the sensor locations and the source locations r'. $\mathbf{q}$ represents the dipole moments (orientation and magnitude). More details about these Kernels and the Leadfield matrix may be found in *Appendix A*.

In general the kernel used in the solution, regardless of the chosen model, may be factored so that the terms independent of the sensor locations may be computed separately to build a so-called transfer matrix, which greatly increases the efficiency of the solution of the inverse problem, as it would normally require the computation of the Leadfield for many source locations. Multiplying this transfer matrix with the primary potential yields the Leadfield matrix G, which is used to compute the current densities during the solution of the inverse problem [34].

2.3 Solving the Inverse Problem

The relationship between the measured scalp potential and the primary source currents may be described mathematically by means of the following expression:

$$\mathbf{M} = \mathbf{G} \cdot \mathbf{D} + \eta \tag{2.2}$$

In this equation, **M** is a matrix that contains the measured EEG information and has N rows (N is the number of sensors), **D** is a matrix containing information on the moments of the dipoles (**D** is used instead of **q** here, to relate it to the current densities (amount of electric current per cross-sectional area), as the orientations are typically fixed to be perpendicular to the border of the gray matter region, as described earlier), **G** is the NxP gain (Leadfield) matrix (with P being the number of dipoles) obtained by solving the forward problem, and represents the scalp potential produced by each current source as measured by the N sensors, and η is an matrix containing the noise of the measurements, assumed to follow a Gaussian distribution $N(\eta|0,(\beta\Sigma_G)^{-1})$, where β^{-1} is a scaling parameter estimated from the stimulus period and Σ_G^{-1} is the noise covariance matrix estimated from the baseline. The full noise covariance matrix $(\beta\Sigma_G)^{-1}$ is assumed to be the variance of the noise.

A wide variety of methods have been developed over the years to solve this problem. These methods may be classified mainly as Parametric (i.e. non-linear Least Squares, Beamformers, Subspace techniques, Computational Intelligence, etc.) or Non-Parametric (i.e. Bayesian Framework, Weighted Resolution Optimization, Shrinking methods, etc.). The category that has been found to yield the best results [36][37] is that of Bayesian methods within the Non-Parametric techniques.

2.3.1 The Bayesian Framework

Bayesian methods applied to brain source localization seek to find an estimator that maximizes the posterior probability distribution of the currents **D** for the observed data **M**, which is represented as the addition of two energy functions: the first energy function is related to the posterior distribution of the measurements **M** given the sources **D** ($p(\mathbf{M}|\mathbf{D})$), whereas the second energy function is associated to the likelihood of the sources (p(**D**)). The formulation of this minimization problem may be found in *Appendix A*.

Several methods exist within this framework, and some of them are frequently used as benchmark for comparing the accuracy of new methods. One of these is the minimum norm estimate (**MNE**), which is characterized by using an L_2 norm loss function combined with Tikhonov regularization as an energy function for the prior information. In practice, this method strives to find values for **D** such that the squared difference between the measurements and the multiplication of the Leadfield times the current densities is minimized. The regularization parameter is used to control the weight given to the prior knowledge, depending on how reliable it is.

Nevertheless, according to Pascual-Marqui [36], this method does not work well with neither the realistic nor the spherical models of the head, as it tends to favor weak and surface sources due to an estimation of the noise [37]. Further improvements have been made on the *MNE* method by adding a weighting matrix based on the norm of the columns of the Leadfield matrix (*weighted MNE*) and by making this weighted estimation recursive, updating the values of the weighting matrix in every iteration.

Other methods have sprouted from *WMNE*, such as the **LORETA** (*Low Resolution Electrical Tomography*) method, which besides using Leadfield Normalization uses a Laplacian operator, which allows it to estimate sources not only on the brain cortex, but within the inner volume. One of the methods found to be most accurate during simulations, often used for comparing new models, is **sLORETA** [36][37], or *Standardized Low Resolution brain Electromagnetic Tomography.* This method uses the estimation obtained from the *MNE* method and standardizes it using its variance, assumed to result from the actual source variance and variation due to noisy measurements. More detailed explanations on all these methods may be found in *Appendix A*.

The VBMEG method is constituted by a static estimation of the current time series and a dynamic estimation of the sources interactions with one another. The static estimation uses an altered version of the MNE method similar in structure to the Wiener filter, which intends to use the current variance to regularize the solution of the L2-reconstruction problem. Nevertheless, because the true current variance is not known, the VBMEG method places a hierarchical prior on the current variance and estimates it iteratively using an Automatic Relevance Determination (ARD) model. The VBMEG method differentiates itself further from the MNE method in that it places a smoothness constraint in the currents, ensuring that neighboring active sources are correlated.

The dynamic estimation, on the other hand, uses a MAR model to determine whether causal interactions exist between active sources found during the static estimation and all other sources anatomically connected to them. The MAR weighting matrix is found using an L2-regularized least-squares method as well, solved using Singular Value Decomposition (SVD).

The sLORETA method, mentioned earlier in this subsection, was used as benchmark for the estimated source locations, and will be shown in the *Results* chapter.

2.3.2 The Multivariate Autoregressive (MAR) Model

The following explanation is based on the work of Harrison and colleagues [38].

Multivariate Autoregressive (MAR) models are an attempt at estimating the values a set of variables will take based on the weighted, linear sum of a number of previous values they have assumed. Such a model has the following form:

$$y_n = \sum_{i\,=\,1}^{m} y_{n-i} \cdot A(i) + e(n) \tag{2.3}$$

In this equation, y_n represents the nth sample of a d-dimensional time series and m is the order of the model, which is equal to the number of previous time samples taken into account. A(i) is a $d \times d$ matrix of weighting coefficients initially assuming causal interactions between the nth time sample of each time series and its preceding m time samples, and e_n is additive Gaussian noise with zero mean. The time series for each variable (from which the mean has been previously subtracted) may be presented in vector form as $x_n = [y_{n\,-\,1}, ..., y_{n-m}]$, which can be expressed in a standard linear regression form, as:

$$y_n = x_n \cdot \mathbf{W} + e_n \tag{2.4}$$

Where W is a $m \times d \times d$ matrix containing the weighting matrices for each time series. Time series may also be placed in matrix form so that it contains the time series of all variables. Therefore, the *MAR* model may be expressed in matrix form as follows:

$$\mathbf{Y} = \mathbf{X} \cdot \mathbf{W} + \mathbf{E}_n \tag{2.5}$$

Where $\mathbf{E}_n$ is a matrix containing the aforementioned Gaussian noise for all time series. In these models, all variables are connected to one another beforehand. The model is then fitted to the data in order to determine which of the coefficients are non-zero. These coefficients are related to the concept of *Granger Causality*, which states that activity in region X "Granger Causes" activity in region Y if any of the connections from X to Y, over all time lags, are non-zero. More details on the MAR model used in the present work will be provided in the next section.

Chapter 3

Methods

The whole estimation process can be followed in **Figure 3.1**. This process is broken down in this section, with more thorough explanations about the calculations shown in *Appendix A*.

3.1 Experimental Data

Real data analyses were performed on data provided by the Vrije Universiteit Medical Center, recorded from 5 participants, from which 3 were stroke patients and 2 healthy controls. Recorded data was comprised of 62-channel EEG measurements collected during a somatosensory stimulation experiment, structural MRI (T1-MRI) and diffusion weighted MRI (DWI) data. This experiment was divided into two conditions, each of which was the perturbation of one brain hemisphere by means of electric stimulation delivered at the index finger of the contralateral hand. Patients were asked to keep their eyes open and blink normally during the experiments. In patients, the first condition was set to be the unaffected hemisphere, whereas for healthy controls the first condition was set to be the dominant hand. The delivered stimulus was defined to be a monophasic anodal electrical pulse with a width of 400 μs, applied at a frequency of 3-4 Hz, randomly distributed over the surface of each index finger. The length of the trial window varied between 250 and 300 ms. The intensity of the stimulation was determined by finding the sensitivity threshold for each patient, which corresponds to the value at which each individual is capable of perceiving 5 out of 10 pulses. The stimulation value was then set to be twice as large as the value corresponding to the sensitivity threshold.

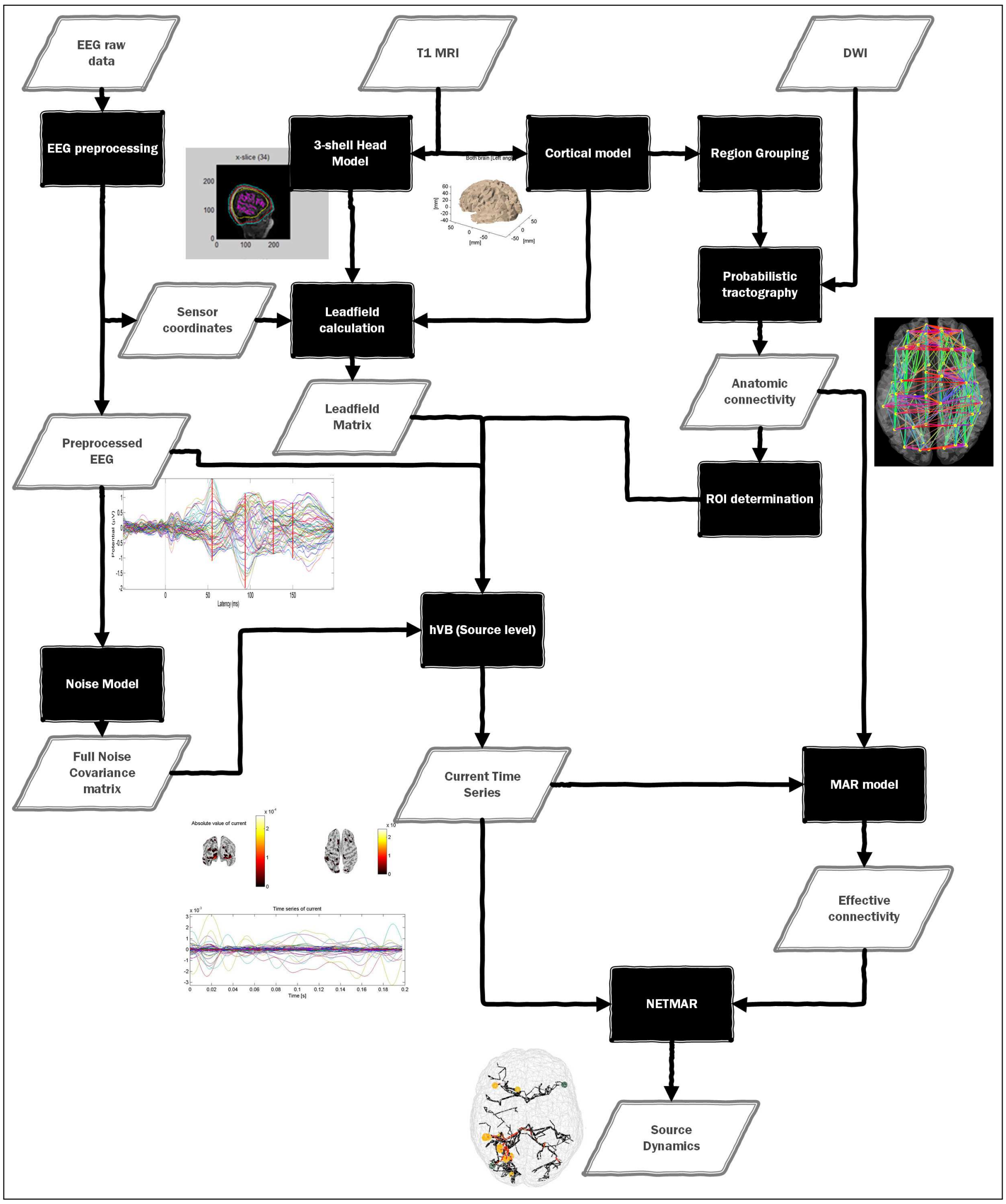

Figure 3.1: VBMEG method pipelines, combining EEG, structural and diffusion MRI to estimate the dynamic interactions between active sources related to a particular stimulus. The preprocessed EEG and the noise model obtained from its baseline are used alongside the calculated Leadfield in the static estimation (hVB) at the source level, so that the estimated currents might be related to the ROI interactions directly. The estimated current time series are included in the MAR model based on the estimated anatomic connections and their corresponding time delays to estimate the effective connectivity (causality) between sources. The 100 strongest pairs of connections are selected, a higher resolution tractography is estimated between them, and a dynamic model of the information flow between active sources is obtained

3.2 Preprocessing

3.2.1 Construction of the Cortical and Head Models

An anatomical model of the patient's head was built, discriminating white from gray matter, so that prospective brain sources could be constrained to lie within the gray matter region exclusively, and the orientation of their magnetic fields set to be perpendicular to its surface. The cortical model, specific to every patient, was built using T1 MRI images corrected using *SPM8* in order to avoid a biased extraction of the cortical surface due to low-frequency variation values derived from the non-homogeneity of the MRI machine's magnetic field [39]. The cortical surface was extracted using *Freesurfer*'s "recon-all" command, which performs motion correction, boundary extraction, corregistration, parcellation, etc. [40].

To solve the *Forward Problem*, a triple-layered realistic model (each layer bearing the conductivity for the scalp, the skull and the brain, asumed to be isometric) was built. The volumetric image of the gray matter used as the innermost shell was obtained using *SPM8*'s "Segment" command, which separates the MRI images into cerebrospinal fluid, white and gray matter [41]. The surface files for the scalp and the skull were obtained using *Freesurfer*'s "watershed" command [40].

3.2.2 EEG Coordinate Transformation

The coordinates and orientations of the sensors (EEG electrodes) were transformed to head coordinates using fiducial markers defined at the approximate location of the left and right preauriculars and the nasion for every participant. The coordinates for these markers were picked manually from the MRI data.

3.2.3 EEG Preprocessing

EEG preprocessing was carried out both in *Matlab* and in *EEGlab*. Matlab was used mainly to remove the stimulation artifact from the raw data, as it is evident enough to be done manually, whereas filtering, epoching, down-sampling, independent component analysis (ICA) and bad component rejection were effectuated directly on *EEGlab*.

The stimulation artifact was removed manually first by identifying the range (across trials) containing its characteristic large spike. The region located within this range was "cut-out" and the gap was reconstructed using *Matlab*'s "fillgaps" function, which uses Autoregressive Modeling to estimate extrapolated values from forward and reverse autoregressive fits [42]. The reconstructed signal was then exported to *EEGlab* for further preprocessing.

The EEG data was filtered using a band-pass filter with lower and upper cutoff frequencies of 1 and 100 Hz, respectively, plus a notch filter at 50 Hz (45-55 Hz) to get rid of the power line noise, with data down-sampling from 2048 to 512 Hz right after. The data was then segmented into 250 ms epochs, going from -50 ms to 200 ms with respect to the stimulus' onset. ICA was applied after epoching to remove components corresponding to EOG (electrooculogram), EMG (electromyogram) and ECG (electrocardiogram) artifacts. Identification of such components was based on concentration of large amounts of activity at an individual electrode and confirmed based on the phase plot for each independent component, where non-artefactual components were identified to be monotonically decreasing. See *Appendix B* for a more thorough explanation on EEG IC rejection.

3.3 Leadfield Calculation

FRESURFER was used to parcellate the cortex into approximately 5,000 elements, which were then grouped into 2000 ROIs using Matlab's "reducepatch" function [43], each with a single current source located at its geometric center. For the calculation of the *Leadfield* at every EEG electrode location, dipoles were set at the vertices of each of the 5,000 elements of the mesh, oriented perpendicularly to the boundary between gray and white matter. A *BEM* was used for the forward computing and was solved with *Galerkin's method* of weighted residuals, using *linear* basis functions to approximate the potential at every surface.

A differentiation between high-resolution, locally distributed sources' currents (dubbed **D**, corresponding to the vertex space) and locally clustered sources' currents (named **Z**, corresponding to the source space) was made, so that the currents **D** was a smoothed version of the currents **Z**, as:

$$\mathbf{D} = \mathbf{W}_L \cdot (\mathbf{Z}) \tag{3.1}$$

Where $\mathbf{W}_L$ is a Gaussian smoothing filter (refer to *Appendix A*). The Leadfield matrix obtained using the dipole locations has a high resolution, which is why it needs be multiplied times the smoothing filter to perform the calculations of the rougher **Z** currents. The relationship between the smooth and the coarse Leadfield matrices is then expressed as:

$$\hat{\mathbf{G}} = \mathbf{G} \cdot \mathbf{W}_L \tag{3.2}$$

The effect of using this smoothed version of the currents is that these sources can be mapped to the vertex space, providing a higher resolution for the location of the activity.

3.4 DWI Analysis

The anatomic connections between brain areas and the time delays corresponding to the lengths of these connections were estimated using probabilistic fiber tracking combining structural T1 MRI and DWI images. The images were acquired by means of a 3T MRI scanner (Discovery MR750, GE Medical Systems), and the dMRI image acquisition protocol involved 40 non-collinear gradient directions uniformly sampled over a sphere, with a b-value of 1000 s/mm^2, with an imaging matrix of 96x64 (zero padded to 256x256).

Image correction for subject motion during acquisition and for Eddy currents was done using *FSL*'s "eddy correct" [44] command, whose bias on the grading direction was compensated by rotating the b-vector using *FSL*'s non-linear registration tool FNIRT [45].

The seed and target ROIs, converted to volume ROIs and transformed to diffusion space, where used for fiber tracking in MRtrix [46] using a fiber orientation distribution reconstructed at each voxel by constrained spherical deconvolution. Fibers were tracked with a step length of 0.2 mm within a mask of white matter volume, generating 10^5 fibers from each ROI and stopping them either when intersecting another region or when being longer than 300 mm. This process is exactly the same as the one done by Fukushima et al. [31].

The estimated connections where evaluated in terms of strength, defined as the number of fibers between a pair of ROIs f_t divided by the number of fibers generated from the pair's corresponding seed ROI f_s, normalized by the size of the regions. This is expressed in the following equation:

$$Conn.Strength = \frac{(f_t/v_t)}{(f_s/v_s)} \tag{3.3}$$

Where v_t and v_s are the number of voxels in the target and in the seed ROIs, respectively. These strengths were then binarized using a threshold value of 10^{-4}. The binary values were used as an indicator of significant connections between brain areas and were used to assign interactions and calculate the delays for the construction of the MAR matrix. Furthermore, connected ROIs where the only ones considered as candidates for the estimation of the current densities.

3.5 Source Reconstruction and Connectivity Estimation

As it was mentioned in the introductory section, the Variational Bayesian Multimodal Encephalography (VBMEG) method was used to reconstruct the sources' current densities and estimate the causality underlying their dynamics. Fukushima et al. [31] have presented results obtained when performing the estimation of these two aspects simultaneously, as the results obtained after performing several simulations appeared to be better than those obtained when applying the steps sequentially. Executing both the source reconstruction and the fiber tracking at the same time was later found to result in distortions under certain circumstances. Therefore, it was decided by the research group at ATR and consequently done so in the presently described work, to perform a two-stage estimation. The first stage consists of estimating the current densities using the static hierarchical Variation Bayesian (hVB) method [47]. Once completed, the second stage uses the static results in the dynamic NETMAR method [31] to estimate the effective connectivity and observe the sources' interactions. Besides avoiding the eventual distortions, this also resulted in a dramatic decrease in computation times, as fiber tracking is only done once.

3.5.1 Static Estimation

The static estimation carried out in the hVB method seeks to reconstruct instantaneous values of the sources' currents at multiple points in time. **Equation 2.2** shows what the issue in reconstructing these currents may be, as the total number of currents that may be reconstructed perfectly equals the number of sensors used in the measurements. The value of the currents may then be approximated by iteratively reducing the difference between the measurements and candidate values assigned to the currents multiplied by the Leadfield, as:

$$E(\mathbf{D}) = \nu \|\mathbf{M} - \mathbf{G} \cdot \mathbf{D}\|^2 + \mathbf{D}' \cdot \Sigma_0 \cdot \mathbf{D} \tag{3.4}$$

ν is a parameter that controls the relative weight between the reconstruction error and the regularization matrix Σ_0, which may contain different sorts of information. For example, choosing the identity matrix as a regularization matrix results in the MNE method mentioned in chapter 2 (and described more in detail in *Appendix A*). The minimum solution to **equation 3.4** is obtained by differentiating it with respect to **D** and making it equal to zero, and is given by:

$$\mathbf{D} = \Sigma_0^{-1} \cdot \mathbf{G}' \cdot \left(\mathbf{G} \cdot \Sigma_0^{-1} \cdot \mathbf{G}' + \nu^{-1}\mathbf{I}_p\right)^{-1} \cdot \mathbf{M} \tag{3.5}$$

A different choice for this matrix might be the current covariance matrix, which would result in the inverse filter known as the Wiener filter. Nevertheless, this method only reconstructs the currents adequately when the current's true covariance matrix is known, which is not the case in practice.

To face this, the hVB method places a hierarchical prior on the current's variance, which is then estimated from the observed EEG data. The method offers the possibility of using fMRI information as prior information on the variance distribution, although this data was not available in the present work and the mean variance was initialized as 1. Additionally, the hVB method places a spatial smoothness constraint based on structural MRI data (T1) that forces closely neighboring sources to have a high correlation with respect to one another, thus enforcing the notion of these neurons firing at the same time. The currents are therefore calculated using the following equation:

$$\begin{aligned} \mathbf{D}(t) &= \Sigma_\alpha^{-1} \cdot \mathbf{G}' \left(\mathbf{G} \cdot \Sigma_\alpha^{-1} \cdot \mathbf{G}' + \beta^{-1} \mathbf{I}_p \right)^{-1} \cdot \mathbf{M}(t) \\ \Sigma_\alpha^{-1} &= \mathbf{W}_L \cdot \mathbf{A}_L^{-1} \cdot \mathbf{W}_L \end{aligned} \tag{3.6}$$

In this equation, Σ_α^{-1} is the diagonal current covariance matrix with the inverse variance (precision) of the currents along its diagonal and β^{-1} is the average noise variance estimated from the baseline of the EEG measurements $\mathbf{M}$. $\mathbf{W}_L$ is a Gaussian filter enforcing the smoothness constraint and A_L^{-1} is the variance matrix of the unsmoothed currents. A more detailed explanation is offered in *Appendix A*.

A consequence of adding the hierarchical prior, which is a nonlinear function of the current's variance, is that the estimation problem cannot be be solved analytically. Therefore, a Variational Bayesian algorithm is used and the minimization problem described by **equation 3.5** is expressed as the maximization of the free energy (see *Appendix A*). Within this framework, the current variance and the current magnitudes are iteratively and alternatively estimated until the free energy converges. The current variance is estimated as a weighted average of the average magnitude of the estimated currents and prior mean variance, as shown in the following expression:

$$\alpha_n^{-1} = \frac{\gamma_{0n\alpha} \cdot \bar{\alpha}_{0n}^{-1} + \frac{T}{2} \left(\frac{1}{T} \sum_{t=1}^{T} \mathbf{D}_n^2(t) \right)}{\gamma_{0n\alpha} + \frac{T}{2} (\mathbf{L}(\Sigma_\alpha^{-1}) \cdot \mathbf{G})_{n,n}} \tag{3.7}$$

Where $\gamma_{0n\alpha}$ is a confidence hyperparameter that controls the width of the gamma function describing the posterior distribution of the currents' variance. The steps for calculating the current densities and updating the variance are summarized in the following pseudocode:

1. Initialization of the current variance α^{-1} and the confidence parameter γ_0. If fMRI information is used, this corresponds to the solution of the Wiener filter in the first iteration. If no fMRI data is available, the variance and the hyperparameter are both initialized as 1, which as the first iteration is equal to the MNE solution
2. Calculate the current magnitudes (**Equation 3.6**)
3. Update the current variance (**Equation 3.7**)
4. Calculate the free energy. If the solution does not converge, re-calculate the current densities and variance, with the mean variance along the diagonal of the current

covariance matrix

The maximization of the free energy is achieved by minimizing the divergence between the true joint posterior distribution of the current densities and their variance given the observed EEG measurements with respect to the trial posterior distribution of the estimated parameters, which once it converges conforms the evidence of the measurements (marginal likelihood) and may be expressed as the minimization of the Kullback-Leibler (KL) distance. A step-by-step description is provided in *Appendix A*.

In any case, the current version of the VBMEG method does not iterate the solution until the free energy converges, but rather a fixed number of 1000 times. A threshold is then applied to the resulting current magnitudes, considering only those above it as active sources related to the EEG data.

3.5.2 Dynamic Estimation

Once the currents' time series had been calculated using the hVB static estimation, they were used in a MAR model to estimate the causality between the ROIs containing the sources found to be active, which may be interpreted as dynamic functional integration between these regions. In *chapter 2*, it was mentioned that the order of the model consists of the number of previous time samples used to estimate the current value of the time series. There are multiple strategies for finding an optimal value for the order, such as the minimum description length (MDL) or a maximum likelihood approach [38]. Nevertheless, the amount of previous samples used is determined differently in the VBMEG method, as it uses the estimation of the fibers connecting ROIs to build a delay matrix containing the information transfer times between sources. The delay for self-interactions was considered to be of 3 ms and the propagation velocity along the axons was set to be 6 m/s. The time series are then clipped according to these delays in order to estimate the MAR coefficients. Under these constraints, the MAR model is meant to constitute a source space representation of the sources' interactions across the whole brain.

A small example of this process is provided here in an attempt to explain how the estimation works. The dynamics of a single source $D_{n,t}$ were modeled as follows:

$$\mathbf{D}_{n,t} = \sum_{k \in C_n} \left(a_{n,k} \cdot \mathbf{D}_{k,t-\delta_{n,k}} \right) + \omega_{n,t} \tag{3.8}$$

In the previous equation, C_n is an index of the sources that are anatomically connected to the nth source, $a_{n,k}$ is the corresponding MAR coefficient and $\delta_{n,k}$ is its time lag for the interconnection between the nth and the kth sources. $\omega_{n,t}$ is the reconstruction error.

Let us assume there are 3 neighboring nodes, 2 of which are connected to the first, as shown in **Figure 3.2**.

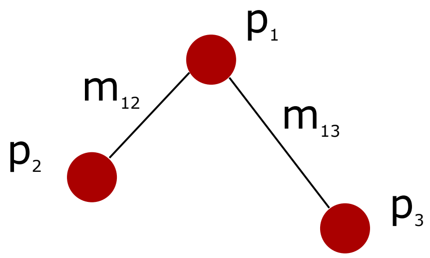

Figure 3.2: Example of three anatomically connected sources $p_1 ... p_3$, separated by a distance m

In order to calculate the MAR coefficients of matrix $\mathbf{A}_1$ for source p_1, its corresponding current time series, here called d_1, is "clipped" so that only the segment of the time series that could, in principle, be explained by the current of any other source is considered. To this end, the largest time lag from the matrix is taken into account, and the current d_1 is set to go from time zero plus the largest time lag, up until the end time minus the same time lag. Within this time range, even the sources located farthest from p_1 could already have had an effect on it. The $\mathbf{D}_{k,t-\delta_{1,k}}$ matrix is built in the same spirit. The first column corresponds to the self-interactions of p_1, so the time lag to be removed is equal to 3 ms. The rest of the columns of $\mathbf{D}_{k,t-\delta_{1,k}}$ contain shortened current time series for the rest of the sources, in this case p_2 and p_3, and the lag is obtained from the estimated fiber length connecting them to p_1, so m_{12} and m_{13}, and the pulse propagation velocity. The $\mathbf{D}_{k,t-\delta_{1,k}}$ matrix includes the shortened currents of all the C_n nodes estimated to be physically connected to node p_1. With the vector d_1 and the matrix $\mathbf{D}_{k,t-\delta_{1,k}}$, it is now possible to calculate the MAR coefficients describing the causality for source p_1 by solving the following least-squares error problem:

$$min(E(\mathbf{A}_1)) = \|\mathbf{D}_1 - \mathbf{A}_1 \cdot \mathbf{D}_{1,t-\Delta_1}\|^2 + \lambda \cdot \mathbf{A}_1^2 \tag{3.9}$$

Where Δ_1 is a matrix containing the lags for all connected sources and λ is a regularization parameter for which an adequate value was found using Akaike's Bayesian Information criterion (ABIC) [48]. The solution is obtained using Singular Value Decomposition (SVD), and the result is a vector with the MAR coefficients for current D_1, from which any found to be non-zero are interpreted as effective connections. The first element of the MAR vector a_1 reflects a relationship from the source with itself and is therefore located at the diagonal of the MAR matrix $\mathbf{A}$, whereas the rest describe remote interactions and are located in the off-diagonal, which constitutes the effective connectivity matrix.

This same procedure is repeated for each current until the MAR matrix is built. The dynamic source model including all sources may be described as:

$$\mathbf{D}_t = \sum_{l=1}^{L} (\mathbf{A}_l \cdot \mathbf{D}_{t-\Delta_l}) + \omega_t \tag{3.10}$$

Once the $\mathbf{A}_l$ matrix has been calculated, multiplying the matrix $\mathbf{D}_{t-\Delta_l}$ containing each of the shortened current time series used before, times the MAR matrix, constitutes the MAR model describing the currents' matrix $\mathbf{D}_t$ (**equation 3.10**). The difference between this $\mathbf{D}_t$ matrix and the MAR model $\mathbf{D}_{t-\Delta_l} \cdot \mathbf{A}_l$ is the residual error ω_t, which may be regarded as an input driving the MAR model. This residual error has a temporal structure that may be used to correct the forecast error when performing a forward prediction of the value of the currents [49]. As such, the residual error was used as an input to the MAR model to predict the value of the currents in order to evaluate the regularization parameter λ, as it was found by the Japanese group to result in divergences when set too low.

The final step of the VBMEG method, dubbed NETMAR, involved a visualization of the information transfer between the regions enclosing the identified active sources. "Strong connections" were identified between these regions and fiber tracking was repeated, taking only these into account. The result is an animation of the source dynamics, from which snapshots at different time points are shown in the next chapter.

Chapter 4

Results

In this section, results for 3 handpicked subjects will be shown. The first one is a healthy control chosen due to the high quality of its EEG data, thought to be a representative benchmark for the capabilities of the VBMEG method when localizing sources related to somatosensory evoked potentials (SEPs), as well as the information transfer using NET-MAR. The second subject is a stroke patient with a Fugl-Meyer score of 63 out of 66 and an EmNSA score of 37, which was considered to be a well recovered patient. The third subject was a patient with a Fugl-Meyer score of 59 and an EmNSA of 35, chosen as a more severe (yet still mild) case of stroke. This setup is meant to provide a comparison between stroke patients and healthy subjects that, even though not large enough to offer representative conclusions about the studied phenomena, might very well serve as an indication of this method's potential for future research.

4.1 Static Estimation Results

Source reconstruction was performed for every time point so that the current time series for each source was estimated. Special attentions was paid to times of interest at the event-related potential (ERP), particularily to sources found at a time point close to P50 (positive ERP spike at 50ms). P5 has been interpreted as reflecting the activation of the contralateral somatosensory cortex during a task triggering SEPs [50]. Besides this time point, approximate times for N70 (negative spike at 70ms), P100 and N140 were taken as reference for comparison with cortical maps existing in the literature. The choice for time points was done by observing the waveform of the C3 and C4 electrodes when the right hand and left hand were stimulated, respectively. These waveforms are shown in **Figure 4.1**, with the time values compiled in **Table 4.1**. **Figure 4.2** shows topographical maps at the time points shown in **Table 4.1**.

At the time point corresponding to the P50 wave landmark, a comparison was made between the topographical maps, an estimation carried out using Pascual Marqui's sLORETA free academic software [51], and the static estimation of VBMEG (hVB), shown in **Figure 4.3**. The topographical maps (bottom row) offer a large area within which active sources would be expected to reside, whereas the estimation performed by sLORETA shows a more specific location for the active sources, albeit of it having a low spatial resolution (middle row). The solution obtained using the hVB (top row), on the other hand, shows physiologically plausible locations for active sources with a much higher degree of specificity. The

Subject	**Right Hand Stim.**				**Left Hand Stim.**				Units
	P50	**N70**	**P100**	**N140**	**P50**	**N70**	**P100**	**N140**	**[Time]**
Control 1	55.66	94.73	127.9	151.4	49.8	84.96	135.7	157.2	ms
Patient 1	53.71	102.5	129.9	174.8	53.71	102.5	124	174.8	ms
Patient 2	55.66	110.4	143.6	155.3	53.71	96.68	110.4	135.7	ms

Table 4.1: Time points corresponding to chosen P-N (positive and negative) wave landmarks, expected to be found around 50, 70, 100 and 140 ms. The time instances were determined by observing the C3 (left hemisphere) and C4 (right hemisphere) electrode measurements (shown in **Figure 4.1**), as their location is above the sensorimotor area stimulated during the experiments

colors in these plots represent the Brodmann areas segmenting the cortex by functional specialization. The sources estimated using the hVB method for all PN time points from **Table 4.1** are shown in **Figure 4.4**.

The accuracy of the estimation was evaluated in terms of the Variance Accounted For (VAF) as in the work of Yoshioka et al. [52], which was calculated using the following equation:

$$VAF = 1 - \frac{\sum_{k=1}^{N} \left(\mathbf{M}_k(t) - \hat{\mathbf{M}}_k(t)\right)^2}{\sum_{k=1}^{N} \mathbf{M}_k(t)^2} \times 100 \tag{4.1}$$

Where $\hat{\mathbf{M}}$ is the estimated EEG from the real measurements $\mathbf{M}$, N is the number of electrodes and t is time going from -50 ms to 200 ms. The obtained VAF for all subjects is shown in **Table 4.2**.

Subject	VAF% Right Hand	VAF% Left Hand
Healthy Control 1	99.9377	99.9999
Patient 1 (FM=63)	91.5956	89.1255
Patient 2 (FM=59)	84.4479	79.6016

Table 4.2: VAF for VBMEG's estimation of the location of active sources

The signal to noise ratio (SNR) was calculated by considering the baseline to contain noise exclusively. The SNR [53] was computed as follows:

$$SNR = \left(\frac{Arms_{signal}}{Arms_{noise}}\right) \tag{4.2}$$

Where *Arms* is the root mean square amplitude. The estimated SNR values for all subjects are shown in **Table 4.3**:

Subject	SNR Right Hand	SNR Left Hand
Healthy Control 1	23.6774 (13.7433 dB)	25.8536 (14.1252 dB)
Patient 1 (FM=63)	14.1981 (11.5223 dB)	9.7563 (9.8928 dB)
Patient 2 (FM=59)	6.1266 (7.8722 dB)	3.7537 (5.7446 dB)

Table 4.3: SNR for preprocessed EEG data used as input in the estimation of the location of active sources. The value in decibels (dB) was calculated as $SNR_{dB} = 10 \cdot log_{10}(SNR)$, and is included for comparison purposes in the discussion section. This scale is useful when dealing with signals having a wide dynamic range[54]

4.2 Dynamic Estimation Results

Source interactions estimated from the MAR model were used in an attempt to observe information flow among brain regions. Sources had to be chosen for testing their connectivity strength with respect to their anatomically connected neighbors, from which a maximum of 100 strong pairs of sources were chosen. **Figure 4.5** shows the estimated anatomical connections over the whole brain and the information transfer between active sources. The time points chosen for the "snapshots" of the source dynamics were those corresponding to the aforementioned PN-waveform landmarks.

4.3 Modularity

A new Brain Module visualization tool designed to perform comparisons between multiple subjects was tested in the present work. This analysis tool, developed by Miguel Ângelo Ribeiro Ferreira Braga[1] at TU Delft, is still under improvement, but it could already show some of its potential for future studies on brain connectivity. The modularity represented in **figure 4.6** shows the estimated groups of densely interconnected sources for each subject, based on the anatomical connectivity matrix obtained during fiber tracking. The visualization tool evaluates the connections between sources and finds an optimum surpassing a pre-specified threshold, which was set to be 1.2. Details on the actual calculations may be found in the work of Newman [55].

---

[1] Developer contact: TU Delft, Mekelweg 2, 2628 CD Delft, Computer Graphics and Visualization group. Phone: +351918885470. *e-mail*:miguelrfbraga@gmail.com

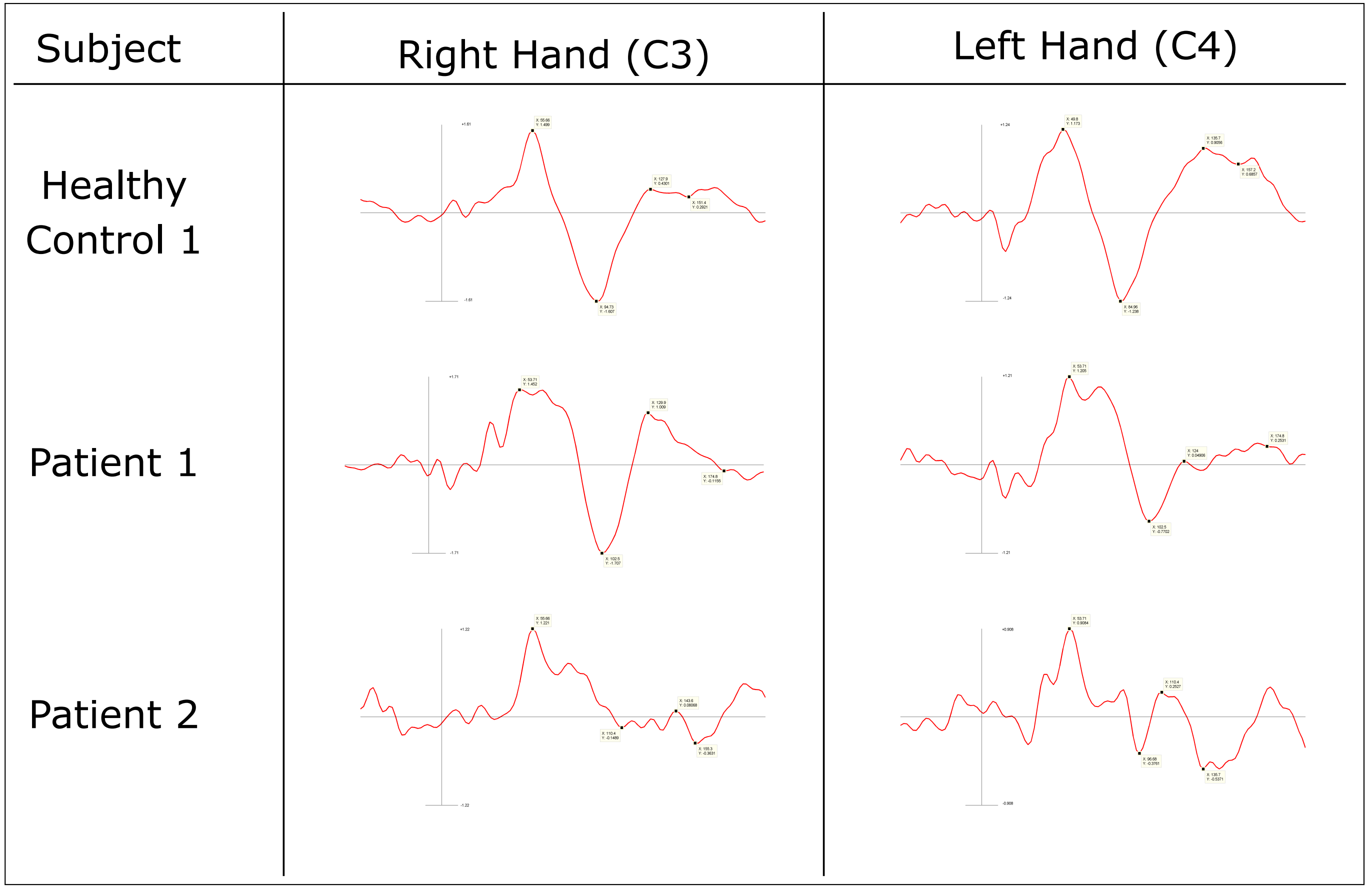

Figure 4.1: Signal at C3 (sensorimotor area, left hemisphere) and C4 (sensorimotor area, right hemisphere) electrode locations, used to identify the time instances corresponding to the PN time points (shown in **Table 4.1**) related to activity of the somatosensory cortex in every subject, as explained in the work of Hämäläinen et al. [50].

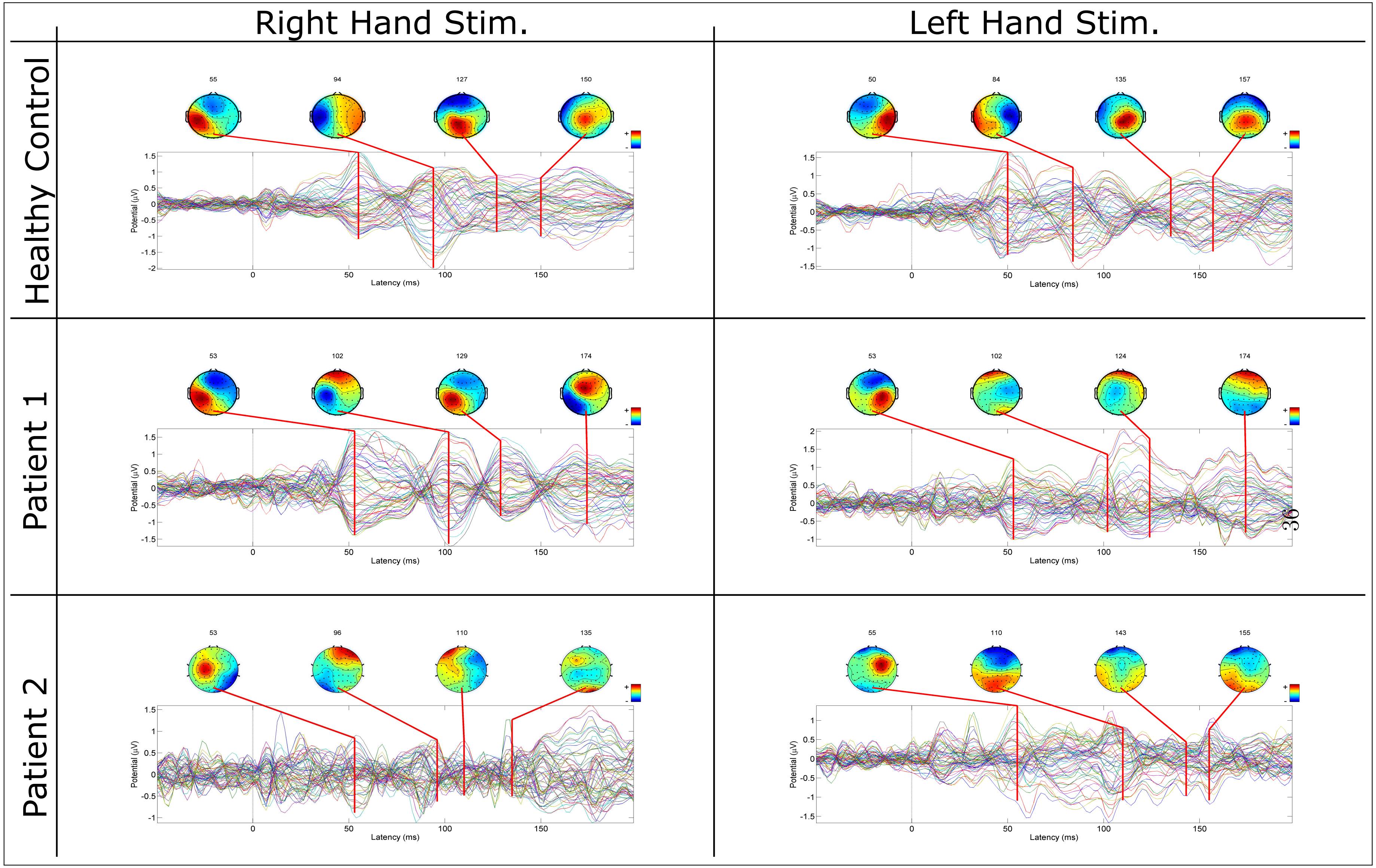

Figure 4.2: EEG for each subject, with topographical plots corresponding to each time instance from **Table 4.1**. Topographical plots are graphical representations of the electrode measurements, interpolated to provide a smooth map of neural activity; each black dot on the map corresponds to an electrode. The shown EEG signal contains the average across trials (500 trials) of all 62 channels used in data acquisition. The averaging improves the SNR and "digs out" the ERP from the noise, as the induced activity is time and phase locked in the signal.

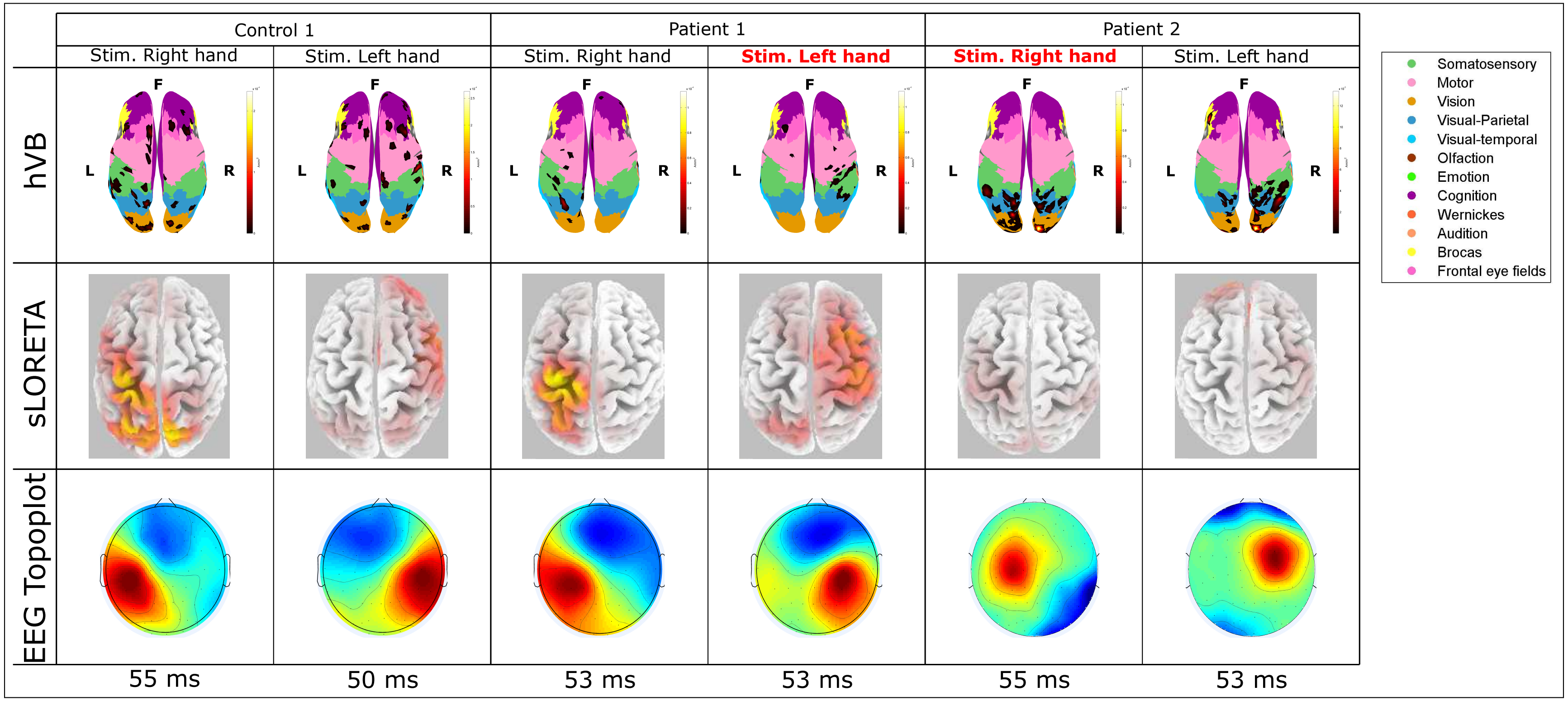

Figure 4.3: Source locations estimated at P50. Comparison between the hVB and sLORETA methods, with EEG topographical plots for reference on stimulated hemisphere. In patients, the stimulated hand highlighted in red corresponds to the affected hand. Colored areas on the cortex correspond to Brodmann areas grouping brain regions by functional specialization.

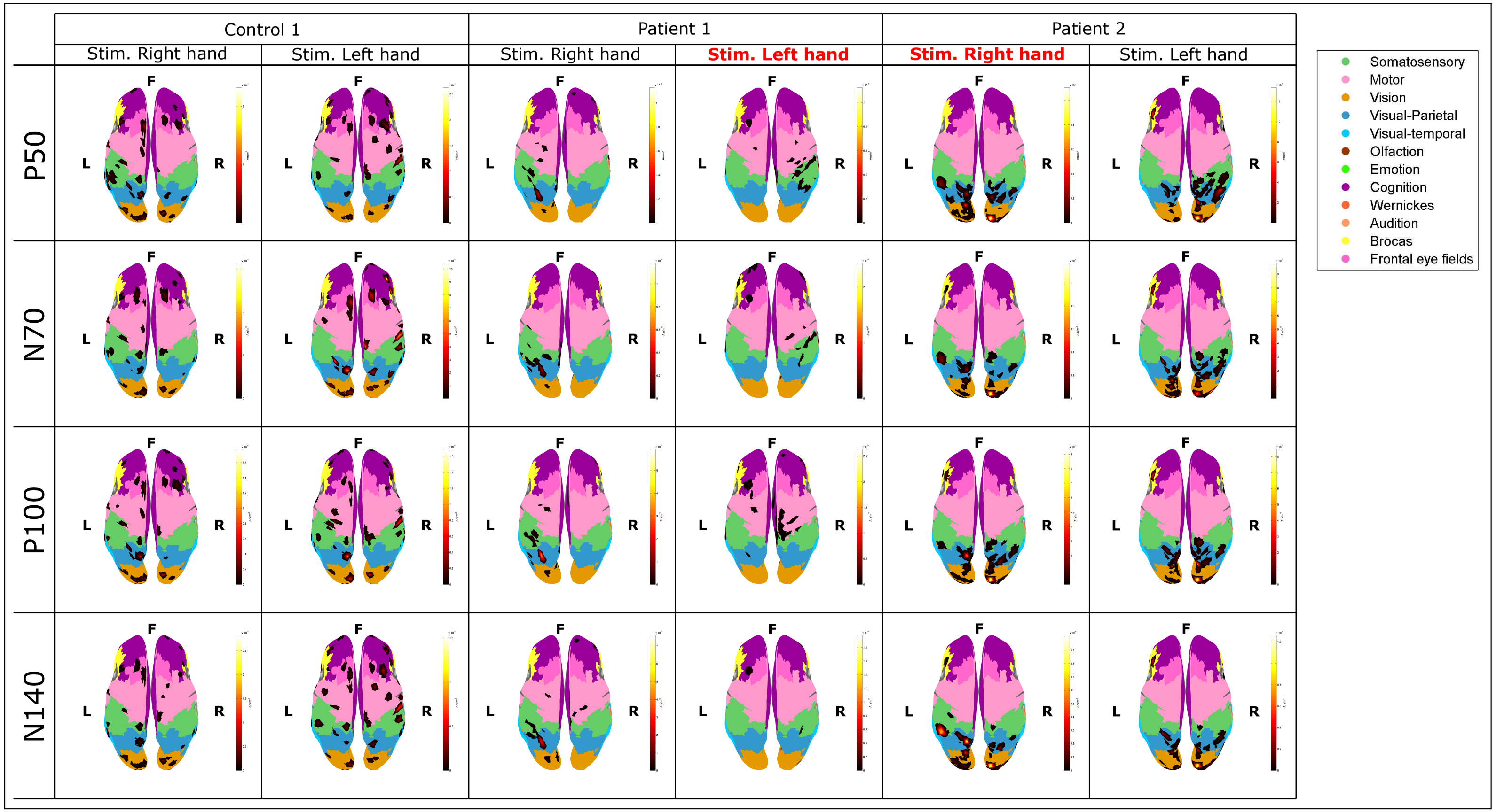

Figure 4.4: Source locations for PN time points of interest. In patients, the stimulated hand highlighted in red corresponds to the affected hand. Colored areas on the cortex correspond to Brodmann areas grouping brain regions by functional specialization. The color bar at the right of each image represents the magnitude of the sources

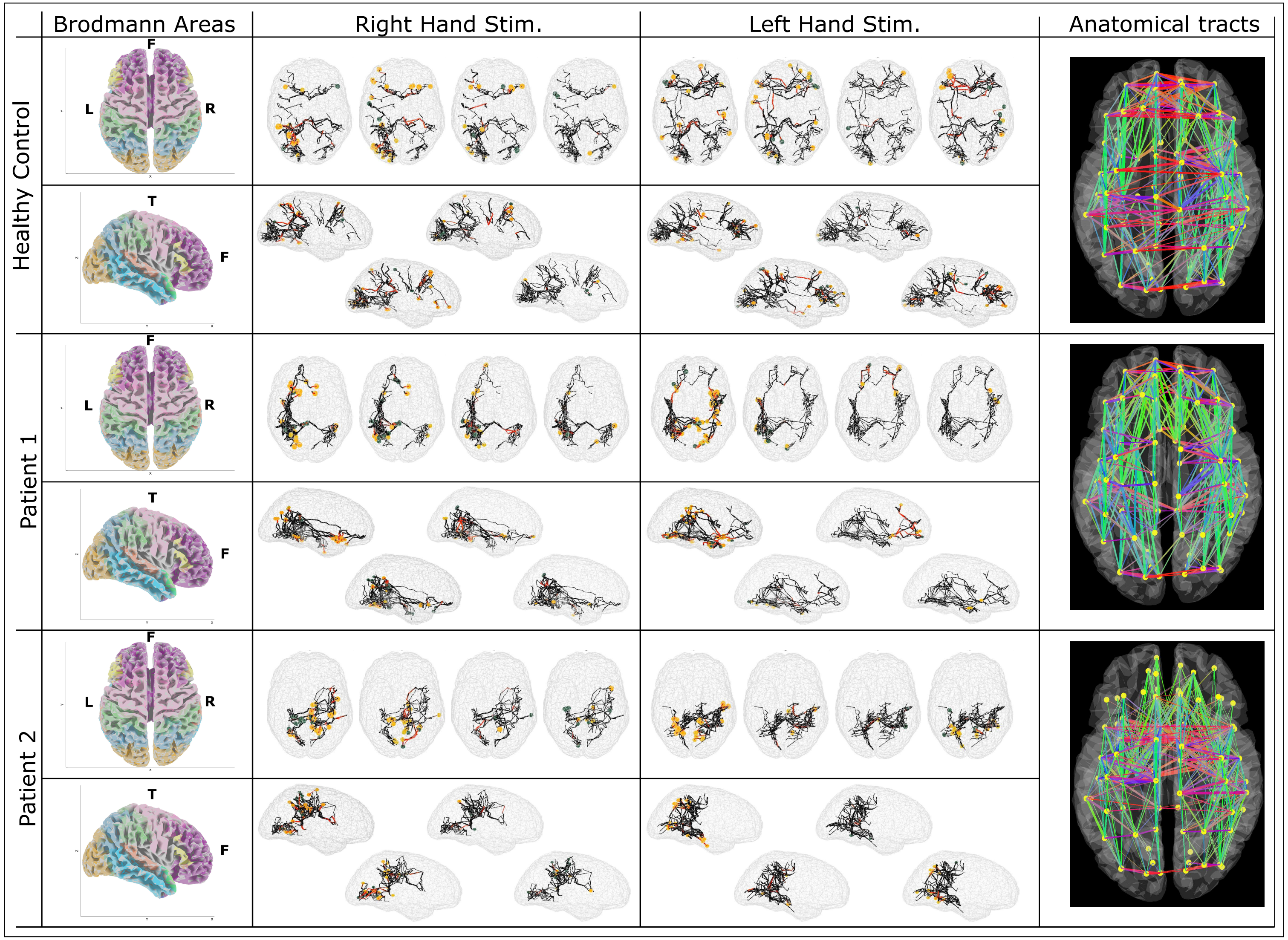

Figure 4.5: Estimated anatomical connections and dynamic transitions inferred from the MAR model. The time instants shown are those from **table 4.1** with the intention of showing information transfer between reconstructed sources of interest. The Brodmann areas shown are the same ones as in **Figure 4.4**, but the cortex looks different because MNI registration is used in this case (to match the cortical representation used in the dynamic model). In the "snapshots" of the source dynamics, yellow circles correspond to active sources, and differences in their diameter reflect their magnitudes. Dark circles are sources at their initial state of activation. Black tracks between sources represent inactive connections, whereas their activity is shown in red

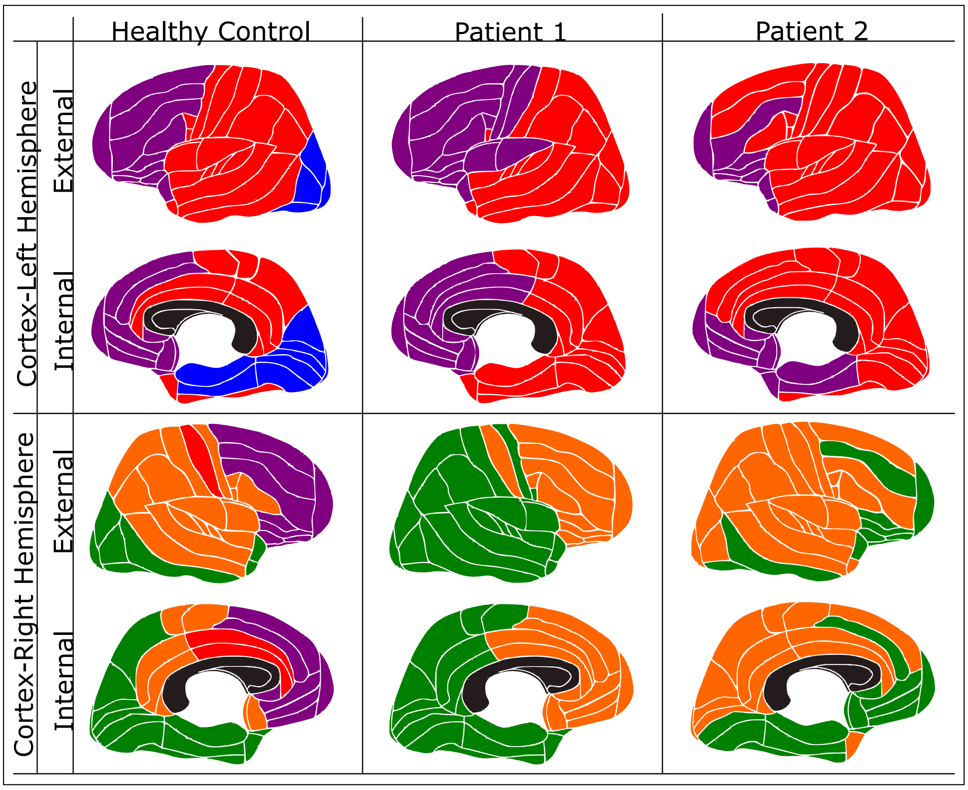

Figure 4.6: Estimated modules for each subject using a modularity threshold of 1.2. Each color corresponds to a module, sometimes present in both hemispheres. The black regions represent the corpus callosum and are not part of any module. For each subject, each color reflects a single module, but are not meant to be compared between subjects

Chapter 5

Discussion

The present work aimed to apply a two-stage estimation procedure, consisting of a static estimation of the location of active sources related to a specific stimulus and a dynamic estimation of the information transfer between them. This application is intended as a proof of concept to support the candidacy of the method in future studies, moving towards an increasingly precise prognostic model of stroke. The assessment of the obtained results is broken down into several main aspects in this section, first enlisted and then (some of them) discussed more in depth.

I. Advantages of this method:

    - The soft prior placed on the current's variance in the static approximation renders the estimation robust against noise, especially when fMRI data is used to initialize the variance
    - The smoothness prior allows for the estimated currents to be mapped to the dipole space, providing a higher spatial resolution to the estimated active areas. The currents' reconstruction, carried out at the source level, can be directly related to the estimation of the interactions between ROIs
    - The estimation of the activation causality between sources provides insight on functional integration between brain areas
    - The selection of strong fiber pairs between estimated sources further constrains the solution, as only sources found to have a causal effect on their anatomically connected neighbors are left, which might remove false positives found during the static estimation
    - The visualization of the information transfer between active sources, based on a higher-resolution tractography focused on the identified strong pairs, provides valuable insight into the topology of the network involved in a specific task

II. Validity of the static estimation: A high VAF was calculated for all subjects, even for those where a poor SNR of the EEG was found

III. Preliminary findings:

    - Estimated source locations: Active sources were found at the expected regions at the time points of interest shown in **Table 4.1**

- White matter pathways: Physiologically plausible pathways were estimated for most subjects, connecting sources in the sensorimotor cortex to the central area of the brain (i.e. thalamus) and to each other between homologous contralateral regions
- The modularity analysis tool succeeded in grouping neural modules consistently, although a formal comparison is complicated at this stage, as the tool is still under development

IV. Challenging aspects:

- Model assumptions: Assumptions on the spatial sparseness and smoothness of the currents, as well as on the noise having a Gaussian distribution and being temporally uncorrelated may not approach reality enough, which may lead to inaccuracies in the estimation
- The noise model: The noise covariance matrix is estimated from the baseline, which is assumed to be conformed only by noise. During the iterative estimation of the current densities and the current's variance, a scaling factor for the noise is estimated from the stimulus period, which is used to adjust the noise model. If the estimated scaling factor was inappropriate, noise could be over or under estimated, which could result in the parameters over-fitting the solution. Additionally, different models for the noise will lead to different estimation results, and as long as a "true model" is not found, there will always be uncertainty regarding the possibility of fitting the noise in the solution
- The reconstruction threshold: The default reconstruction threshold was too high, as it was a value equal to 5% of the largest current reconstructed. Sources found in the visual cortex, consistently found to have larger magnitudes, obscured sources in all other areas in many cases. A threshold taking into account 5% of sources possessing the largest magnitudes was used instead, which resulted in a consistent within-subject estimation of sources in the expected areas
- The MAR model choice: This model might be an oversimplification of the dynamic interactions between brain regions, as it does not include input and noise dynamics. Furthermore, its linear character does not include effects resulting from the joint activity of multiple areas, which most likely exist in the brain
- Nonlinearities: The coupling in the somatosensory feedback has been found to be nonlinear. However, the linear method used for the static estimation seems to estimate the current densities appropriately. It might be the case that the short latency of the stimulus used in the present work generates an approximately linear response, which might not be the case when using a continuous form of stimulation, such as a multisine signal
- SNR differences: Differences in SNR between subjects obstruct a direct comparison between them, as it is hard to know whether observed differences in the

estimation are due to the brain characteristics of the subjects (i.e. patients) or due to a low SNR. Nevertheless, comparisons between conditions (between brain hemispheres) are possible within patients, as consistent results were found in both of them. This could be useful in longitudinal studies, in case the low SNR was characteristic in stroke patients

V. Recommendations:

  - The fMRI-based prior: Whenever a reliable prior derived from fMRI data is available, the weighting of the estimation may be shifted towards the prior knowledge to a larger extent, which empowers the ARD model and reduces the risk of the parameters over-fitting the model
  - Computation requirements: Some stages of the estimation process, such as the estimation of the white matter tracks, require a lot of computation time. This did not result in large problems in the present work, as only a few subjects were processed, but parallel computing might be necessary for larger studies, involving many participants
  - Experimental setup: Data acquisition must be performed with care, so that a large SNR may be achieved and meaningful results may be obtained. Additionally, trial design must be done in such a way that the effects of the stimulation of the previous trial has already died out, so that they don't overlap

5.1 Model Validity

The VAF was calculated for the results of the static estimation of each subject. In general, values were high and coincided with the values reported by Yoshioka et al.[52]. They reported that, when correct prior information was used, VAFs larger than 90% were calculated. These results were compared to the used range of the hyperparameters used in the hierarchical prior, and the large VAF values were seen when the values of the hyperparameters had medium to high values (placing a mild and a high confidence in the fMRI prior). In the present work, these values were set to 1, as no fMRI information was available. Therefore, the large values found (especially the one close to 100) could have more than one interpretation.

One interpretation could be that the noise is being underestimated and the parameters are over-fitting the solution, estimating the noise. If this was the case, there are some options that could be tried. One of them, a bit questionable, could be to fix the noise covariance matrix to be the one initially calculated from the baseline, skipping the iterative update of the noise scaling factor. The other option, would be to use one of the main advantages of this method, which is to use the t-values of the fMRI data to initialize the currents variance. In this way, the ARD model can "prune" low-variance sources much more effectively, reducing the risk of over-fitting.

Another interpretation, could be that the variance estimation was done really well. In an ideal case, having the true current variance would lead to an exact estimation of the current densities. This would also imply that the noise estimation was very accurate. The calculated SNRs for all subjects might hint towards this, as high values were obtained for the subjects with highest VAFs. Babiloni et al. [56] mention that EEG recordings may have SNR values ranging from 10 to 20 when performed during highly synchronized and spatially focused events, such as evoked potentials from the primary sensory cortex. Luck [57] mentions that a reasonable EEG SNR is of about 10, and Parks et al. [58] show some examples of signals with different SNRs (in decibels), where it can be seen that a 5 dB SNR corresponds to a still noisy signal (like the one found in patient 2), and that an SNR of 10 dB looks indeed quite clean. Therefore, the high VAF, alongside a high SNR and within-subject consistency could indicate that the estimation was indeed accurate. In any case, the addition of the fMRI prior is most likely convenient.

5.2 Preliminary Findings

5.2.1 Location of active sources

The expected source locations for time points related to activity of both the primary (SI) and secondary (SII) somatosensory cortices for the healthy control were based on the work of Hämäläinen et al. [50], where they reported the following areas:

1. P50: Interpreted as reflecting the activation of the contralateral SI somatosensory cortex
2. N70: Generated in the contralateral SI somatosensory area
3. P100: Reflects contralateral and ipsilateral activation of the SII somatosensory cortices
4. N140: Bilateral but asymmetrical, showing larger presence on the contralateral side

Table 5.1 shows the percentage of active sources that were estimated to be in the sensorimotor cortex and in the visual-related areas (this last region shown as it was found to consistently contain a large amount of sources, an aspect that will be relevant when discussing thresholds later on).

The percentage of sources found in the somatosensory area at P50 for the Healthy Control does show presence of active sources in the contralateral side to the stimulated hand, which also holds for N70. The bilateral activation expected at P100 can be seen, although it is not symmetric, and the expected asymmetric activation at N140 can indeed be seen in the percentages.

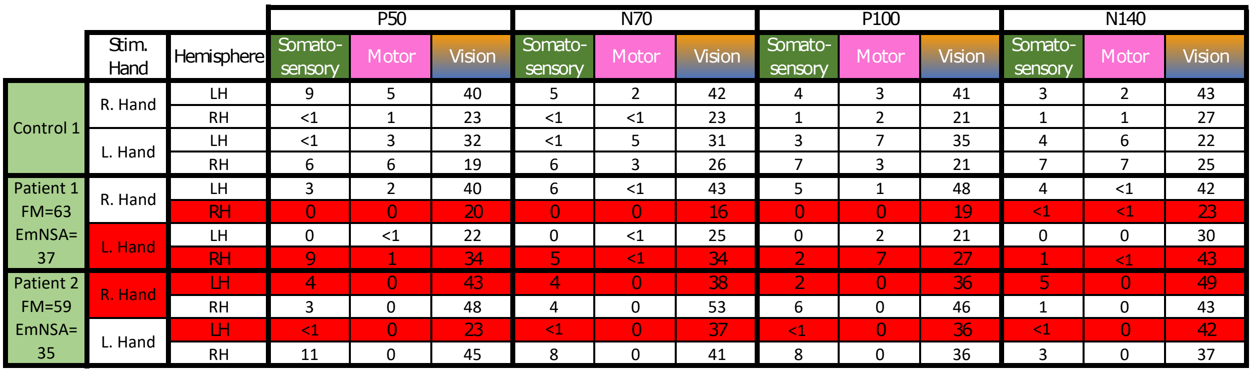

			P50			N70			P100			N140		
	Stim. Hand	Hemisphere	Somato-sensory	Motor	Vision	Somato-sensory	Motor	Vision	Somato-sensory	Motor	Vision	Somato-sensory	Motor	Vision
Control 1	R. Hand	LH	9	5	40	5	2	42	4	3	41	3	2	43
		RH	<1	1	23	<1	<1	23	1	2	21	1	1	27
	L. Hand	LH	<1	3	32	<1	5	31	3	7	35	4	6	22
		RH	6	6	19	6	3	26	7	3	21	7	7	25
Patient 1 FM=63 EmNSA= 37	R. Hand	LH	3	2	40	6	<1	43	5	1	48	4	<1	42
		RH	0	0	20	0	0	16	0	0	19	<1	<1	23
	L. Hand	LH	0	<1	22	0	<1	25	0	2	21	0	0	30
		RH	9	1	34	5	<1	34	2	7	27	1	<1	43
Patient 2 FM=59 EmNSA= 35	R. Hand	LH	4	0	43	4	0	38	2	0	36	5	0	49
		RH	3	0	48	4	0	53	6	0	46	1	0	43
	L. Hand	LH	<1	0	23	<1	0	37	<1	0	36	<1	0	42
		RH	11	0	45	8	0	41	8	0	36	3	0	37

Table 5.1: Percentage of active sources found in the somatosensory, motor and visual Brodmann areas. This percentage is taken from the top 5% sources, assumed to be active as a consequence of the applied stimulation. The visual percentage contains the visual, visual-temporal and visual-parietal areas. The cells highlighted in red correspond to the affected hemispheres and hands of patients

The case of the stroke patients might be more difficult to compare. At a first glance, it seems like Patient 1 does satisfy the expectations for P50 and N70, but the bilateral activation expected at P100 and N140 is not seen, which could be related to the apparent decrease in inter-hemispheric connections observed in **Figure 4.5**. On the other hand, Patient 2 shows a symmetric bilateral activation when the affected hemisphere is stimulated, which seems to be a frequent finding in post-stroke cases [59] [60]. There are too few subjects in the present work to draw such conclusions, but the consistent finding of sources in the somatosensory cortex might be an indicator of the potential of this method in future studies.

5.2.2 Pathways

Knösche et al. [61] used manganese tracing as benchmark for white matter tracts estimated using different methods, mentioning this technique still faces issues related to manganese diffusion into extracellular space and crossing fibers, to name some of them. Nevertheless, the general areas attributed to tracks sprouting from the sensorimotor cortex were used to make a rough comparison with the estimated effective tracks found for the healthy control in the present work. The routes related to the motor and the somatosensory cortices expected to be found were [61]:

1. Motor Cortex: Cortico-thalamic tract to the ventral-anterior/ventral-lateral nucleus, cortico-striatal tract to the caudate nucleus and a cortico-cortical tract connecting the motor cortices on both hemispheres, crossing the mid-body of the corpus callosum
2. Somatosensory Cortex: Cortico-nigral tract ending in the substantia nigra, cortico-thalamic tract terminating at the ventral-posterior/ventral-posterior-lateral nucleus,

and a cortico-cortical tract connecting both somatosensory cortices, propagated through the genu of the corpus callosum

A visual inspection of the tracks shown in **Figure 4.5** shows that these pathways could indeed have been estimated for the healthy control, although the exact locations of each tracks' extremes must be verified. Nevertheless, the connections do seem to lead to the center of the brain, where the expected structures would be, and the cortices of both hemispheres seem to be connected. A frontal view of these could make the comparison much easier in future work. The estimated pathways in the healthy control may be appreciated with relative ease, but this is not the case for stroke patients. The tracks estimated for patient 2 do seem to lead to the corpus callosum, but those for patient 1 rather seem to lead away into the frontal lobe. The high degree of validity of the solution obtained for the healthy control is a good indicator of this estimation, as the effective tractography currently discussed is based on the sources found to be active, but more exploratory work is needed before any conclusions about the accuracy of this estimation may be made.

5.2.3 Estimated Modules

The modularity analysis tool mentioned in Chapter 4 estimated five modules for the healthy control and four for the patients when a threshold of 1.2 was used. Defining an adequate threshold for module definition is an important topic of research in the characterization of brain networks [62], which is why it is complicated to compare the modules obtained thus far, as threshold adjustments may be required for stroke patients. Found modules group together regions related to multiple different tasks, such as sensorimotor and visual signal processing, and even though brain networks seem to be widespread (which may explain why focal damages often affect a wide array of functions) [63], this groups are yet to be validated. Meunier et al. [64] carried out a study comparing the modularity of young people (18-33 years old) to that of elderly people (62-76 years old), finding 5 modules in the first group and 6 in the second. In the present work, even though the applied tool defined 5 modules for the healthy control as well, some of them (i.e. central module) are very similar on both hemispheres, which in the work of Meunier et al. [64] are grouped in the same module. Nevertheless, central, frontal and posterior modules were identified for the healthy control, failing to identify the ventral frontal and medial temporal reported in the aforementioned study. In the case of stroke patients, only two very large modules where identified, which may suggest a need to try higher threshold values when dealing with patients.

5.3 Challenging Aspects

5.3.1 Model Assumptions

The VBMEG method is built upon a series of assumptions that may not be entirely accurate and that may influence the estimation results to a large extent, which should be taken into account during their interpretation. Some of these assumptions include spatial sparseness and smoothness of the dipole currents, a time invariant current variance within each trial, an accurate cortical model obtained from structural images (i.e. T1 MRI) and a correct corregistration between EEG and structural MRI coordinates [52]. From these, one assumption that might be particularly compromised in the present work is the corregistration, as one of the steps includes manually selecting the fiducial markers (preauriculars and nasion) from MRI images. A measure used to assess this selection is the mean scalp forcing distance, which was considered to be acceptable when around 5 mm, following ATR's advice. Nevertheless, a possible way of improving the estimation in this sense is using automatic algorithms such as Iterative Closest Point (ICP) [65].

When these assumptions are not met by the actual data, estimation errors might most likely occur. Nevertheless, it has been reported [31][47][52] that the estimation greatly improves when adding the fMRI prior to the current's variance, as long as the hyperparameters are well tuned depending on the task involved, which improves the robustness of the method against assumption errors and noise [52].

5.3.2 The noise model

A particularly sensitive assumption involved in the solution implemented by the VBMEG method is the one taken upon the nature of the noise present in the signal. In this method, noise is assumed to follow a Gaussian distribution with zero mean, and the noise covariance matrix used as a regularization factor is estimated from the baseline assuming time samples to be serially uncorrelated, thus assuming the baseline to be constituted entirely by noise. Different assumptions for the noise, such as representing it as the variance of the signal across trials or the remnant of subtracting the ERP from each trial, will result in different outcomes.

Regardless of what portion or aspect of the signal is assumed to be noise, assuming it to be uncorrelated may also not always be accurate. Actually, the estimation done with the NETMAR method seems to indicate the noise is correlated in some cases. As this method considers the baseline to be noise, having causal relationships between sources occurring within this range could be interpreted as the baseline not being comprised of noise exclusively, which was observed in some of the animations of the source dynamics. Future work may be focused on exploring the effects of building the noise model in an alternative way.

5.3.3 The Reconstruction Threshold

An important factor for the discrimination of active sources related to the stimulus in question is the threshold for excluding weak sources. The threshold used by the Japanese group is equal to 5% of the magnitude of the largest reconstructed current. Nevertheless, this threshold was too high for the present study and sources on the somatosensory cortex were found only in a couple of subjects. Instead, a threshold leaving the top 5% of the reconstructed currents with largest magnitudes was used. As it can be seen in **Figure 5.1**, a large amount of sources was consistently found in the vision-related regions using this threshold, which means that active sources in the visual areas were consistently found to have large magnitudes. This is probably due to the fact of participants having their eyes open during the experiment.

The 5% of the maximum current threshold might have worked for the Japanese group because they used the method on data related to a face recognition task and were thus looking for sources in these regions. In the case of the present work, active sources on the sensorimotor areas seem to have a much lower magnitude than sources in the visual area, which is why the default threshold did not work for all subjects.

Therefore, the exclusion threshold must be defined carefully, especially when there are no expectations for the location of the sources [66]. There are alternative methods, such as Beamforming approaches, which filter out sources automatically [37]. One of these methods, called Linearly Constrained Minimum Variance (LCMV) beamformer was used as benchmark by Fukushima et al. [31], but results were found to be less accurate after running simulations, as sparse source distributions were not correctly estimated and more false positives were returned.

Another option could be to try using an L_1-norm instead of an L_2-norm as a regularization term, which provides a sparser solution by minimizing the sum of the absolute values of the currents. However, Silva et al. [67] carried out a comparison between these two options, and found that L_1 norms were more sensitive to noise and more computationally expensive, as the number of grid points considered in the analysis must be increased for larger numbers of electrodes.

5.3.4 MAR model choice

The MAR model is an attractive option for exploring interesting phenomena pertaining to the dynamics of the brain, as it provides insight on functional integration over the brain related to a specific task and local neighbor interactions, while remaining relatively simple to implement and solve [38][48]. Leaving the evident limitation of this model being linear aside, for the time being, and that it may very well fail to describe the nonlinear brain dynamics accurately, other issues remain, even if the brain dynamics were linear.

The construction of the MAR matrix depends on the chosen order for each time series, which corresponds to the number of previous time samples to be taken into account as a linear combination to represent a given value. In the present work, the order for each current time series was defined by shortening the time series of physically connected sources, depending on the distance between them. In concept this makes sense, but the way in which these distances and their corresponding time delays were determined might not reflect the characteristics of the information transfer accurately enough, resulting in an inadequate comparison between multiple time series. In other words, this approach relies heavily on the tractography performed, which adds an extra aspect to evaluate when validating the estimation of the source interactions. The study of the specifications of the applied commands for fiber tracking was beyond the scope of the present work, but it might be an interesting line of research in future endeavors.

5.3.5 Nonlinearities

The hierarchical prior placed on the current variance turns the inverse problem into a nonlinear problem. The VBMEG method approaches the solution by means of an iterative optimization of the Free Energy, which was found by Sato [68] to be equivalent to the natural gradient method [47]. However, the problem being a nonlinear function of the current's variance does not make VBMEG a nonlinear method. The sensory feedback in the nervous system has been found to be coupled in a nonlinear way [69], which is why it might be surprising for this linear method to be a ble to estimate the location of active sources accurately. A possible explanation is that the short latency of the electrical impulses used to generate the SEPs causes an approximately linear response. Nevertheless, this may be a problem when dealing with continuous perturbations, such as multisines.

On the other hand, the estimation on the source dynamics is performed with a linear MAR model, which was found to result in false positive estimates on the effective connectivity during simulations done by Fukushima et al. [31]. Therefore, alternatives must be considered to model these aspects more precisely. Possible additions to the present processing scheme could be the use of bi-linear variables, which model hypothesized interactions between variables (i.e. change of connection strength between two sources as an effect of changes in a third source, or the relationship between the currents and an extra factor such as time) [38].

5.4 Recommendations

5.4.1 Computational requirements

A laptop computer with an i7 processor with 4 cores, 3.60 GHz and 16 GB of RAM was used, running Matlab 2014a for compatibility reasons with the Japanese method. **Table 5.2** shows the approximate computation times for each stage. Tractography took much longer for patients than it did for controls (about 60% more time), and had to be performed in a Linux environment, which was installed in a virtual machine on the same laptop. While tractography took between 1.5 and 2.5 days with two cores assigned to that task exclusively, computation times can be dramatically reduced with the use of a computer cluster (i.e. INSY cluster at TU Delft). This was not done in the present work due to a lack of time, as it would be necessary to adapt the code so that it might work properly with the architecture of the cluster.

Task	Computation time
Leadfield Matrix	00:05:30
Current's reconstruction	00:00:08
MAR model	00:00:25
Whole brain tractography	1.5 to 2.5 days
Strong-pairs tractography	03:00:00

Table 5.2: Computational times for all tasks in hh:mm:ss format

As more comprehensive studies, aimed at drawing conclusions about the observed phenomena, will require processing many subjects, parallel computing may very well be necessary. Investing time in adapting the program to be run at a computer cluster will turn the heaviest processes into a trivial matter.

5.4.2 Experimental setup

A total of 16 data sets were made available for the present work. During the EEG preprocessing stage, it became evident that most of these were infested with noise and bad channels and were, therefore, not useful for processing. This was not a real problem for the presently discussed endeavor, as it was more of a proof of concept, but future work searching to draw meaningful conclusions about the observed phenomena should pay special attention to the data acquisition stage. A good idea could also be to add an electrode for detecting eye artifacts (i.e. above one of the eyes).

Additionally, it might be beneficial to have longer time spans for each trial, as effects from areas related to somatosensory stimuli may yet be present after the 200 ms characterizing the data used in this study (i.e. P300 at approximately 300 ms [50]).

Further, the convenience of EEG over other techniques (i.e. MEG) is its low cost and the relative portability of the equipment (i.e. the 4D-EEG [70] project equipped a van with EEG recording equipment to visit patients and perform measurements). Being so that fMRI data seems to have a large impact in the estimation accuracy and that this data is not so easily acquired, it might be interesting to look at alternatives in this area. For example, Sato et al. [71] reported to have found similar results using Near Infrared Spectroscopy (NIRS) as those obtained from fMRI measurements, which could prove to be an inexpensive and portable option for future studies.

5.5 Future work and potential impact

The results obtained during the presently described research effort constitute evidence of the potential of this method in studying structural and functional changes in stroke patients. However, there are still many aspects to explore before meaningful conclusions about the observed phenomena may be drawn such as the impact of using different noise models in the solution. For example, as it might be of interest to study brain activity related to mechanical stimuli and this might involve continuous perturbations (i.e. multisine), it will be necessary either to define a range to be considered as the baseline (the VBMEG method estimates the Noise covariance matrix from it) or to extract some alternative form of noise from the continuous signal. Furthermore, this sort of stimulation might require altering the method to account for nonlinearities (i.e. nonlinear least squares).

Furthermore, there may still be space for improvement in the solution of the Forward Problem, as better fits for the sensor registration than the ones obtained may yet be achieved. Additionally, a high quality of the EEG data must be sought so that meaningful results may be generated. As it was briefly mentioned earlier in this chapter, a deeper study of the tractography and its validity may be paramount, due to the large influence it has in the estimation of the source dynamics.

On the other hand, a MAR model may be too simplistic to adequately describe the brain dynamics, which is why an MARX (exogenous) or the use of an M-ARMAX model instead could improve the estimation dramatically, as they would model the effects of the input as well and, in the case of the ARMAX structure, even include disturbance dynamics [72].

As it is right now, this method could prove to be a useful tool at observing the effects of rehabilitation on stroke patients in a more direct fashion. Ward [73] carried out a review on the rehabilitation therapies applied at present and reached the conclusion of the main issue being that these are not planned according to the underlying mechanisms of recovery, failing to tend to the specific needs of each individual in many cases. Further work on this method could lead to a better understanding of brain plasticity, which could one day pose the possibility to trigger it at will and in specific ways.

Chapter 6

Conclusions

The VBMEG method applied in the present work consists of a variety of pipelines that interact towards the estimation of active sources and their dynamics, related to a particular stimulus. Each of these pipelines embodies a whole research topic, as their use is based on assumptions and simplifications that may reduce the degree of fidelity of the model to different extents. Consequently, much work is needed in all areas involved before conclusive statements may be made regarding the observed phenomena. However, the high scores in the used measures for estimation validity, alongside the apparent consistency in the estimation of the source locations at time points where somatosensory activity was expected, provides evidence of the value and the potential of this method in the study of the brain. Furthermore, even though a MAR model may be an oversimplified representation of the source dynamics, it does seem to be a valuable tool to be built upon.

Overall, this work built a dynamic model portraying the information flow related to SEP stimulation both in healthy controls and in stroke patients. To do so, high spatial resolution information from MRI and DWI was used to complement the EEG data, characterized by a high temporal resolution. Furthermore, this is the first application of the VBMEG method to SEP data, and its promising results bear witness to this method's value for future explorations. Therefore, it is reasonable to state that further research along this line towards a better understanding of neural dynamics is justified.

Acknowledgments

I would like to thank Frans van der Helm for allowing me to participate in this research endeavor and supporting my candidacy for the task, as well as Mitsuo Kawato for facilitating the collaboration between TU Delft and ATR. From ATR, I would like to thank Noriko Masui for all her help in my settling in during my internship, Okito Yamashita for his support, enabling and guidance, and Yusuke Takeda for his instruction, patience and aid. Special thanks to Ryosuke Hayashi and Nushi-san, without whose direct help and excellent attitude this paper would perhaps not have come to be as it is. From TU Delft, my heartfelt thanks to Yuan Yang and Lena Filatova, for sharing their knowledge and skills, making this experience far more enriching than it would have been otherwise. Special thanks to Miguel Braga for adapting his analysis tool to the needs of this work and for sharing it to complement the results presented here. My gratitude goes as well to the TU Delft and the CONACYT, for the opportunity to broaden my horizons and further develop my career.

Appendix A

Brain source localization and Dynamic Estimation

A.1 Solution to the Forward Problem

The mathematics explained in this section were based mainly on the work of Mosher et al.[34].

The relationship between the magnetic field **b** and the current densities **j** of a group of sources is shown by the Biot-Savart law, shown next:

$$\mathbf{b}(\mathbf{r}) = \frac{\mu_0}{4\pi}\int_G \mathbf{j}(\mathbf{r'}) \times \frac{\mathbf{d}}{d^3} d\mathbf{r'} \tag{A.1}$$

Where $\mathbf{d}$=$\mathbf{r}$-$\mathbf{r'}$ (with magnitude d) is the distance between the observation point $\mathbf{r}$ and the source point $\mathbf{r'}$, and $\mathbf{j(r')}$ corresponds to the current density at the source points. The integration is executed over the closed volume G; outside this volume, both the current and the conductivity are set to be zero. μ_0 is the permittivity of empty space.

The currents in the previously shown volume integral consist of two components, the passive $\mathbf{j^v}$ and the primary $\mathbf{j^p}$ currents. This distinction is made in order to phrase that the passive currents, which are a result of the macroscopic electric field in the conduction medium of the volume, arise from neural activity (primary currents) in a certain region. This is shown in the following expressions for both current components.

$$\mathbf{j}^v(\mathbf{r}) = \sigma(r)\mathbf{E}(\mathbf{r}) \tag{A.2}$$

$$\mathbf{j}^p(\mathbf{r}) = \mathbf{j}(\mathbf{r}) - \mathbf{j}^v(\mathbf{r}) \tag{A.3}$$

Where σ is the conductivity of each layer and $\mathbf{E}$ is the electric field, which when assuming the magnetic field to be quasi-static, is equal to the negative gradient of the electric potential, as $\mathbf{E} = -\nabla v(\mathbf{r})$, as explained by Hämäläinen et al.[74]. Substituting $\mathbf{j(r)}$ in Biot-Savart's law yields the following expression:

$$\mathbf{b}(\mathbf{r}) = \frac{\mu_0}{4\pi}\int_G (\mathbf{j}^p(\mathbf{r'}) - \sigma(\mathbf{r'})\nabla v(\mathbf{r'})) \times \frac{\mathbf{d}}{d^3} d\mathbf{r'} \tag{A.4}$$

This volume integral may be rewritten as a sum of surface integrals in order to take into account the conductivity of each layer (corresponding to each type of tissue)[74], as follows:

$$\mathbf{b(r)} = \mathbf{b}_{\infty}(\mathbf{r}) - \frac{\mu_0}{4\pi} \sum_{i\ =\ 1}^{S} (\sigma_i^- - \sigma_i^+) \cdot \int_{S_i} v(\mathbf{r'})\mathbf{n}_i\ (\mathbf{r'}) \times \frac{\mathbf{d}}{d^3} d\mathbf{r'} \tag{A.5}$$

Where n_i is a vector perpendicular to the ith surface, oriented outwards, and the "+" and "-" superscripts indicate the conductivity outside and inside the ith surface, respectively. The variable S is the number of surfaces into which the cortex is divided. The primary field is the magnetic field observed at a certain location r due to the primary current exclusively, and it's defined as:

$$\mathbf{b}_{\infty}\ (\mathbf{r}) = \frac{\mu_0}{4\pi} \int_G \mathbf{j}^p(\mathbf{r'}) \times \frac{\mathbf{d}}{d^3} d\mathbf{r'} \tag{A.6}$$

With a corresponding primary potential v_{∞} :

$$v_{\infty}\ (\mathbf{r}) = \frac{1}{4\pi\sigma_0} \int_G \mathbf{j}^p(\mathbf{r'}) \cdot \frac{\mathbf{d}}{d^3} d\mathbf{r'} \tag{A.7}$$

Where σ_0 is the unit conductivity of an infinite homogeneous medium. The primary potential and the primary field may be calculated by specifying a current distribution $j^p(\mathbf{r'})$. In order to compute the magnetic field as shown in **equation A.5**, it is also necessary to compute the potential as shown below:

$$\sigma_0\ v_{\infty}(\mathbf{r}) = \frac{\sigma_i^- + \sigma_i^+}{2} v(\mathbf{r}) + \frac{1}{4\pi} \sum_{i\ =\ 1}^{S} (\sigma_i^- - \sigma_i^+) \cdot \int_{S_i} v(\mathbf{r'})\mathbf{n}_i\ (\mathbf{r'}) \cdot \frac{\mathbf{d}}{d^3} d\mathbf{r'} \tag{A.8}$$

Equations A.5 and **A.8** constitute the boundary integral equations for solving the forward problem for external magnetic fields (MEG) and scalp potentials (EEG) on all surfaces, respectively.

A.1.1 The Leadfield Matrix

Let us consider the variable m to be either the the magnetic field or the scalp potential at any given dipole on the cortex. This value, which is found using either **equation A.5** or **A.8**, depending on the measurement technique, is a function of the location, orientation and current magnitude of the dipoles on the cortex, and the location of the sensors used to capture their activity, as expressed by the following equation:

$$\mathbf{m}(\mathbf{r}) = g(\mathbf{r}, \mathbf{r'}, \Theta) \cdot \mathbf{c} \tag{A.9}$$

Where c is the current magnitude and Θ is the dipole orientation. This expression can be extended to take into account the contributions of all dipoles as a linear superposition, as shown in the following expression:

$$\mathbf{m} = \begin{bmatrix} m(r_1) \\ \vdots \\ m(r_N) \end{bmatrix} = \begin{bmatrix} g(r_1, \mathbf{r'}_1, \Theta_1) & \dots & g(r_1, r'_p, \Theta_p) \\ \vdots & \ddots & \vdots \\ g(r_N, r'_1, \Theta_1) & \dots & g(r_N, r'_p, \Theta_p) \end{bmatrix} \begin{bmatrix} c_1 \\ \vdots \\ c_p \end{bmatrix}$$

$$= \mathbf{G}(r'_i, \Theta_i) \cdot \mathbf{C}^T \tag{A.10}$$

Where **G** is the gain (Leadfield) matrix relating the set of p dipoles to the N sensors. This expression may be extended to include the time series of the currents, as the Leadfield matrix is independent from the measurements (which is done in the currently used method)[29].

A.1.2 The Boundary Element Method (BEM)

The explanations provided on this section are based mainly in the work of Mosher et al.[34].

As it was mentioned earlier in this section, **equations A.5** and **A.8** are the boundary equations that will be used in the *BEM*. For the solution of the EEG *Forward Problem*, it is the primary potential v_∞ in equation **A.8** that is known and the task is to find its corresponding scalp potential. Equation **A.8** may be expressed as $L(v(\mathbf{r})) = v_\infty(\mathbf{r})$, where $L(\cdot)$ is a linear operator. Therefore, the task becomes to minimize the difference between L(v($\mathbf{r}$)) and the primary potential. The method used to solve this in the VBMEG algorithm is **Galerkin's method** (discussed shortly), which is a particular sort of **Weighted Residuals** method. In general, *Weighted Residuals* methods add a weighting function w($\mathbf{r}$) to the previously mentioned minimization problem as an inner product for both potentials ($(\cdot,\cdot)$ denotes inner product). This is shown in the following equation:

$$(w(\mathbf{r}), v_\infty(\mathbf{r})) = (w(\mathbf{r}), L(v(\mathbf{r}))) \tag{A.11}$$

In BEM, this weighting function is defined as a finite combination of S basis functions $\psi_s(\mathbf{r})$, as:

$$w(\mathbf{r}) = \sum_{s=1}^{S} \chi_s \cdot \psi_s(\mathbf{r}) \tag{A.12}$$

These equations are both known and linearly independent. Values for χ are chosen arbitrarily such that the weighting function comprehends the entire dimensional space comprised by S, which is the number of basis functions determined by the number of tessellated surfaces. *Note: In Mosher et al.[34], s is called n and S is called N, but for variable consistency across this paper I have renamed them.* This results then in the basis functions providing weighting to the potentials, like:

$$(\psi_i(\mathbf{r}), v_\infty(\mathbf{r})) = (\psi_i(\mathbf{r}), L(v(\mathbf{r}))), i = 1, ..., S \tag{A.13}$$

In this equation, the potential v($\mathbf{r}$) itself is still unknown, but the BEM approaches it as a similar sum as the one used for the weighting function, with nodal parameters v_s, which are a function of the nodes located at $\mathbf{r}_s$, and basis functions $\phi_s(\mathbf{r})$:

$$v(\mathbf{r}) \cong \sum_{s=1}^{S} v_s \cdot \phi_s(\mathbf{r}) \tag{A.14}$$

The choice of the basis functions for the weighting and for the potentials may vary, but what characterizes *Galerkin's method* is that the chosen weighting basis functions are the same as the potential basis functions $(\psi_i(\mathbf{r}) = (\phi_i(\mathbf{r}))$.

Substituting **equation A.14** in **equation A.13** yields the general form of the BEM:

$$\begin{bmatrix} (\psi_1(\mathbf{r}), v_\infty(\mathbf{r})) \\ \vdots \\ (\psi_S(\mathbf{r}), v_\infty(\mathbf{r})) \end{bmatrix} = \begin{bmatrix} (\psi_1(\mathbf{r}), L(\phi_1(\mathbf{r})) & \dots & (\psi_1(\mathbf{r}), L(\phi_S(\mathbf{r})) \\ \vdots & \ddots & \vdots \\ (\psi_S(\mathbf{r}), L(\phi_1(\mathbf{r})) & \dots & (\psi_S(\mathbf{r}), L(\phi_S(\mathbf{r})) \end{bmatrix} \begin{bmatrix} v_1 \\ \vdots \\ v_S \end{bmatrix} \tag{A.15}$$

There are two common choices for basis functions in *Galerkin's method*, *constant* and *linear*. *Constant* refers to the value of the potential being 1 at the centroid of each triangular element covering the cortex, whereas *linear* consists in defining three basis functions for each point within every triangular element. These linear basis functions, used in the VBMEG method as well, are defined as:

$$\begin{aligned}\phi_i(\mathbf{r}) &= \frac{\mathbf{r}\cdot(\mathbf{r}_j\times\mathbf{r}_k)}{\mathbf{r}_i\cdot(\mathbf{r}_j\times\mathbf{r}_k)}\\ \phi_j(\mathbf{r}) &= \frac{\mathbf{r}\cdot(\mathbf{r}_k\times\mathbf{r}_i)}{\mathbf{r}_i\cdot(\mathbf{r}_j\times\mathbf{r}_k)}\\ \phi_k(\mathbf{r}) &= \frac{\mathbf{r}\cdot(\mathbf{r}_i\times\mathbf{r}_j)}{\mathbf{r}_i\cdot(\mathbf{r}_j\times\mathbf{r}_k)}\end{aligned} \tag{A.16}$$

Where **r** is a point inside the triangle and r_i , r_j and r_k are the vertices of a triangle arranged in such way that the permutation from r_i to r_j and from r_j to r_k is a an outward vector from the surface. When *constant* basis functions are used, the number of basis functions S is the same as the number of P dipoles, but when the *linear* basis functions are used, the number of basis functions equals S = P/2+2.

These basis functions, which are to be used both on the weighting and the potential functions, may be substituted in equation **equation A.15**, and this equation can, in turn be expressed as:

$$\mathbf{g} = \mathbf{H}\mathbf{v} \tag{A.17}$$

In this equation, **g** is a Sx1 vector containing the inner product of the basis functions and the primary potentials, **H** is a SxS matrix that is a function of the known basis functions and the head geometry, and **v** is a Sx1 vector containing the nodal parameters v_s . Solving for the nodal parameters yields the following equation:

$$\mathbf{v} = \tilde{\mathbf{H}}^{-1}\mathbf{g} \tag{A.18}$$

$\tilde{\mathbf{H}}^{-1}$ is used instead of $\mathbf{H}^{-1}$ to state that the former is a directly invertible matrix. Substituting in **equation A.14** allows for the unknown potentials to be calculated as:

$$v(\mathbf{r}) \cong [\phi_1(\mathbf{r}),\ldots,\phi_S]\mathbf{v} = [\phi_1(\mathbf{r}),\ldots,\phi_S]\tilde{\mathbf{H}}^{-1}\mathbf{g} \tag{A.19}$$

A.1.3 Matrix Kernels

In **Chapter 2**, it was mentioned that the primary potential may be expressed as a field kernel **k** multiplied by the dipole moments **q**. These factoring may be implemented directly on g_i , as the inner product of the basis functions and a kernel (chosen depending on the type of model built), multiplied times the dipole moments, as shown below:

$$\mathbf{g} = \mathbf{G}_{\infty}\mathbf{q} = \begin{bmatrix} (\psi_1(\mathbf{r}), \mathbf{k}_{\infty}(\mathbf{r}, \mathbf{r'}))^T \\ \vdots \\ (\psi_S(\mathbf{r}), \mathbf{k}_{\infty}(\mathbf{r}, \mathbf{r'}))^T \end{bmatrix} \mathbf{q} \tag{A.20}$$

For an EEG BEM model, the choice of the Infinite Homogeneous Model $\mathbf{k}_{\infty}$ is:

$$\mathbf{k}_{\infty}(\mathbf{r}, \mathbf{r'}) = \left[\tfrac{1}{4\pi}\tfrac{\mathbf{d}}{d^3}\right] \ , where \ \ \mathbf{d} = \mathbf{r} - \mathbf{r'} \tag{A.21}$$

Then, the EEG *Forward Problem* is solved as:

$$v(\mathbf{r}) \cong [\phi_1(\mathbf{r}), \ldots, \phi_S \ (\mathbf{r})]\tilde{\mathbf{H}}^{-1}\mathbf{G}_{\infty} \ \mathbf{q} \tag{A.22}$$

Which can be substituted in **equation A.5** to solve the MEG *Forward Problem.*

As mentioned before, the $\tilde{H}^{-1}$ matrix is independent of the sensor and dipole locations, and may be obtained efficiently using LU decomposition. For this reason, it can be precomputed and then used to calculate the Leadfield matrix for each dipole. The BEM kernel shown before may be expanded to include all N electrodes, as shown below:

$$\begin{bmatrix} \phi_1(\mathbf{r}_1), \ldots, \phi_S(\mathbf{r}_1) \\ \vdots \\ \phi_{N+1}(\mathbf{r}), \ldots, \phi_S(\mathbf{r}_{N+1}) \end{bmatrix} \tilde{H}^{-1}G_{\infty} \tag{A.23}$$

Multiplying this expression times a switching matrix **SW**, which subtracts the (n+1)th electrode from n single ended electrode locations generates the transfer matrix $\mathbf{T}_v$, mentioned in **section 2**.

$$\left(\mathbf{SW}\begin{bmatrix} \phi_1(\mathbf{r}_1), \ldots, \phi_S(\mathbf{r}_1) \\ \vdots \\ \phi_{N+1}(\mathbf{r}), \ldots, \phi_S(\mathbf{r}_{N+1}) \end{bmatrix} (\mathbf{LU})^{-1}\mathbf{G}_{\infty}\right) = \mathbf{T}_v\mathbf{G}_{\infty} \tag{A.24}$$

A.2 Solution to the Inverse Problem

A.2.1 The Bayesian Framework

This explanation on the Bayesian framework is based on the work of Grech et al.[37].

The methods comprising this category seek to find the current densities $\hat{\mathbf{D}}$ that maximize the posterior distribution of $\mathbf{D}$ given the measurements contained in $\mathbf{M}$.

$$\hat{\mathbf{D}} = \max_{\mathbf{D}}[p(\mathbf{D}|\mathbf{M})] \tag{A.25}$$

According to Bayes' law, the conditional probability density of the current densities given the measurements may be defined as:

$$p(\mathbf{D}|\mathbf{M}) = \frac{p(\mathbf{M}|\mathbf{D})p(\mathbf{D})}{p(\mathbf{M})} \tag{A.26}$$

If a Gaussian distribution is assumed for the previously shown posterior density, it can be expressed as:

$$p(\mathbf{D}|\mathbf{M}) = \frac{\exp\left[-F_\alpha(\mathbf{D})\right]/z}{p(\mathbf{M})} \tag{A.27}$$

In this expression, z is a partition function working as a normalization factor (see the *Intermezzo* on this matter) and $F_\alpha(\mathbf{D})$ is:

$$F_\alpha(\mathbf{D}) = U_1(\mathbf{D}) + \alpha L(\mathbf{D}) \tag{A.28}$$

Where $U_1(\mathbf{D})$ is an energy function associated to p($\mathbf{M}|\mathbf{D}$), L($\mathbf{D}$) an energy function associated to p($\mathbf{D}$) and α is a regularization parameter. This means that the maximization problem shown in **equation A.25** may be expressed as the minimization of these energy functions:

$$\hat{\mathbf{D}} = \min_{D}(F_\alpha(\mathbf{D})) \tag{A.29}$$

Intermezzo: The Partition Function as a Normalization Constant

---

This brief discussion of the Partition Function as a normalization constant is based on[75][76].

The probability of a single candidate source having a certain value, defined as the fraction of the sources having that particular value, is located somewhere between 0 and 1, and this probability is mutually exclusive to the probability of it having any other value. At the same time, the probability of a source having *any* value between zero and one, inclusive, is 1. Therefore, the joint probability for the source's possible values must be equal to one, as:

$$P_0 + P_1 + P_2 + ... = \sum_i P_i = \sum_i \frac{n_i}{n} = 1$$

A probability distribution that follows the previous equation is said to be normalized. It is then possible to express this probability as some factor ξ (normalization constant) multiplying a function, like:

$$P_i = \xi f(i)$$
$$\sum_i P_i = \xi \sum_i f(i) = 1$$

Solving for the normalization constant gives a partition function scaling f(i):

$$\xi = \frac{1}{\sum\limits_i f(i)}$$

Coming back to **equation A.28**, $U_1(\mathbf{D})$ may be defined as the least-square reconstruction error (L_2 norm loss function), as long as noise is assumed to be white (temporally uncorrelated, having a Gaussian distribution and zero mean).

$$U_1(\mathbf{D}) = \|\mathbf{GD} - \mathbf{M}\|^2 \tag{A.30}$$

L($\mathbf{D}$), on the other hand, may be defined to contain priors derived from anatomical (i.e. DTI) and functional (i.e. fMRI) data, such as:

$$L(\mathbf{D}) = U_s(\mathbf{D}) + U_t(\mathbf{D}) \tag{A.31}$$

With s and t standing for a spatial and a temporal prior, respectively.

Therefore, the problem of maximizing the posterior distribution of the current densities becomes a minimization problem for the energy:

$$\hat{\mathbf{D}} = \min_D(F_\alpha(\mathbf{D})) = \min_D(\|\mathbf{GD} - \mathbf{M}\|^2 + \alpha L(\mathbf{D})) \tag{A.32}$$

Which shows that it is possible to directly control how strongly the estimation rests on the prior knowledge.

The reconstruction error U_1 is associated to the probability of the measurements $\mathbf{M}$ given the current densities $\mathbf{D}$ in a directly proportional way. For display purposes, the variable $\mathbf{X}$ will be used, being $\mathbf{X} = \mathbf{GD} - \mathbf{M}$:

$$p(\mathbf{M}|\mathbf{D}) \propto \exp(-\mathbf{X}^T.\mathbf{X}) \tag{A.33}$$

Which may be expressed more generally as:

$$p(\mathbf{M}|\mathbf{D}) \propto \exp(-Tr(\mathbf{X}^T.\Sigma^1.\mathbf{X})) \tag{A.34}$$

Where "Tr" is the trace of the matrix and Σ^1 is the data covariance matrix.

Within the Bayesian Framework, there are some methods that are often used as benchmark for the results obtained by newer methods (and combinations of these are used to develop new methods as well). A brief explanation of some of these methods, involved in the present work, will be described next.

Minimum Norm Estimates (MNE)

One of the most used methods, in its most basic form, seeks to find the solution with minimum power and uses Tikhonov regularization. In Tikhnonov regularization, $L(\mathbf{D}) = \left\|\mathbf{D}^2\right\|$, which results in the following expression for $F_\alpha(\mathbf{D})$:

$$F_\alpha\left(\mathbf{D}\right) = \left\|\mathbf{GD} - \mathbf{M}\right\|^2 + \alpha\left\|\mathbf{D}\right\|^2 \tag{A.35}$$

This expression can then be transformed (the proof may be found in the Appendix of Grech et al.[37]) so that the estimation for the current densities is:

$$\hat{\mathbf{D}}_{MNE} = \mathbf{G}^T(\mathbf{GG}^T + \alpha\mathbf{I}_N)^{-1}\mathbf{M} \tag{A.36}$$

Where N is the number of electrodes. The inverse operator $\mathbf{G}^T(\mathbf{GG}^T + \alpha\mathbf{I}_N)^{-1}$ may be expressed simply as $\mathbf{T}_{MNE}$, which when multiplied times the Leadfield matrix yields the resolution matrix $\mathbf{R}$, which should ideally be the identity matrix (corresponding to the current densities being estimated exactly[36]).

To compensate for the partial favoring of weak and surface sources, it is possible to add a weighting matrix, here dubbed W_{MNE}, which is defined as:

$$\mathbf{W}_{MNE} = \Omega \otimes I_3 \tag{A.37}$$

Where $\otimes$ is the Kronecker product (see intermezzo for explanation). Ω is defined as:

$$\Omega_{\beta\beta} = \sqrt{\sum_{\alpha\,=\,1}^{N} \mathbf{v}(\mathbf{r}_\alpha, \mathbf{r'}_\beta) \cdot \mathbf{v}(\mathbf{r}_\alpha, \mathbf{r'}_\beta)^T},\ for\ \beta = 1, ..., p \tag{A.38}$$

Where $\mathbf{v}(\mathbf{r}, \mathbf{r'})$ is the potential measured at the electrode located at position $\mathbf{r}$ with respect to the dipole located at position $\mathbf{r'}$.

Intermezzo: Kronecker products

This brief explanation is based on[77]. If A is a mxn matrix and B is a pxq matrix, the Kronecker product of these matrices is defined as:

$$A \otimes B = \begin{bmatrix} a_{11}\mathbf{B} & \dots & a_{1n}\mathbf{B} \\ \vdots & \ddots & \dots \\ a_{m1}\mathbf{B} & \dots & a_{mn}\mathbf{B} \end{bmatrix}$$

The addition of this weighting matrix constitutes the **WMNE** method, or the *Weighted Minimum Norm Estimates*, whose expression for the estimation of the current densities looks as follows:

$$\hat{\mathbf{D}}_{WMNE} = (\mathbf{W}_{MNE}^T \mathbf{W}_{MNE})^{-1} \mathbf{G}^T (\mathbf{G}(\mathbf{W}_{MNE}^T \mathbf{W}_{MNE})^{-1} \mathbf{G}^T + \alpha \mathbf{I}_N)^{-1} \mathbf{M} \tag{A.39}$$

Further improvements on this method have been made by iteratively estimating the current densities, providing weightings based on the magnitudes of the sources of the previous iteration (*WMNE with FOCUSS*). The weighting matrix $\mathbf{W}_{MNE}$ is normalized using the Leadfield (Leadfield Normalization), which is then described by:

$$\mathbf{W}_{MNE_i} = diag\left(\frac{1}{\|\mathbf{G}(:,j)\|}\right) \mathbf{W}_{MNE_{i-1}}\ diag(\mathbf{D}_{i-1}) \tag{A.40}$$

The estimation then is the same as for *WMNE*, but calculating the weighting matrix in every iteration.

Low Resolution Electrical Tomography (LORETA)

In this method, the Leadfield normalization described earlier is combined with the Laplacian operator Δ, which is a dot product of two gradient vector operators[78], in order to provide sources both on the surface and within the volume the same chance of being reconstructed, as sources are located not only on the cortex, but also inside the brain. The regularization parameter is defined as:

$$\begin{aligned} L(\mathbf{D}) &= \|\Delta \mathbf{B}.\mathbf{D}\|^2 \\ \mathbf{B} &= \Omega \otimes \mathbf{I}_3 \end{aligned} \tag{A.41}$$

Which then results in the following expression for the estimation of the current densities:

$$\hat{\mathbf{D}}_{LOR} = (\mathbf{B}\Delta^T\Delta\mathbf{B})^{-1}\mathbf{G}^T(\mathbf{G}(\mathbf{B}\Delta^T\Delta\mathbf{B})^{-1}\mathbf{G}^T + \alpha\mathbf{I}_N)^{-1}\mathbf{M} \tag{A.42}$$

In the same way as described earlier, there is a recursive version of *LORETA*, called *LORETA with FOCUSS*.

Standardized Low Resolution brain Electromagnetic Tomography (sLORETA)

This method uses the estimation obtained from the *MNE* method and standardizes it using its variance. The variance of this estimate is assumed to result from the actual source variance $\mathbf{S}_D = \mathbf{I}_{3p}$ and variation due to noisy measurements $\mathbf{S}_M^{noise} = \alpha\mathbf{I}_N$. The variance of the electrical potential is then defined as:

$$\mathbf{S}_M = \mathbf{G}\mathbf{S}_D\ \mathbf{G}^T + \mathbf{S}_M^{noise} \tag{A.43}$$

And the variance of the estimated current density is:

$$\mathbf{S}_{\hat{D}} = \mathbf{T}_{MNE}\ \mathbf{S}_M\ \mathbf{T}_{MNE}^T = \mathbf{G}^T[\mathbf{G}\mathbf{G}^T + \alpha\mathbf{I}_N]^{-1}\mathbf{G} \tag{A.44}$$

Which is equivalent to the resolution matrix T_{MNE} mentioned after discussing **equation A.36**. The standardized current density power is then:

$$\hat{\mathbf{D}}_{MNE,l}^T\ \{[\mathbf{S}_{\hat{D}}]_{ll}\}^{-1}\ \hat{\mathbf{D}}_{MNE,l} \tag{A.45}$$

Where $\hat{\mathbf{D}}_{MNE,\ l}$ is a 3x1 vector containing the estimate for the current density at dipole l and $[\mathbf{S}_{\hat{D}}\ ]_{ll}$ is the lth diagonal block of the resolution matrix.

A.2.2 The hierarchical Variational Bayesian (hVB) method

The explanation of this section is based in the work of Sato et al.[47] and the subsequent publication of Yoshioka et al.[52].

As it was mentioned in the sections focused on the *Bayesian Framework* in this appendix, the problem to be solved consists of minimizing the difference between the reconstructed and the measured currents, as enunciated in **equation A.35**. **Equation A.36**, which constitutes the solution to the *Inverse Problem* using the *MNE* method, may be expressed more generally as:

$$\mathbf{D} = \Sigma_0^{-1}\mathbf{G}'\left(\mathbf{G}\Sigma_0^{-1}\mathbf{G}' + \beta^{-1}\mathbf{I}_M\right)^{-1}\mathbf{M} \tag{A.46}$$

Where Σ_0^{-1} is a regularization matrix. Using the identity matrix as a regularization parameter results in the *MNE* method described earlier (equation **A.20**), but varying this regularization parameter results in different linear inverse methods. This regularization term is introduced with the intention of constraining the solution to face the underdetermined nature of the inverse problem that has been discussed before. As the maximum amount of sources that can be estimated exactly is equal to the number of sensors being used, multiplying the Leadfield times an NxN regularization matrix will constrain the solution to this number. The challenge is, then, to define an adequate regularization matrix so that the sources are effectively reconstructed.

A different option for a regularization matrix is the covariance matrix (like in the *Wiener filter*). If the true covariance matrix was known, the source currents could be reconstructed perfectly, but this is not the case. Therefore, assumptions must be made so that a covariance matrix may be built to provide an acceptable approximation of the current densities.

What characterizes the *hVB* method is that it estimates the current variance from the measured EEG signal and uses it to build a regularization matrix to constrain the solution of the inverse problem. This matrix is built using a hierarchical prior on the current variance for the diagonal terms.

Hierarchical Prior

First, a Gaussian prior distribution is assumed for the currents, as:

$$P_0(\mathbf{D}_{1:T}|\alpha) \propto \exp\left[-\frac{1}{2}\sum_{t=1}^{T}\mathbf{D}'(t)\mathbf{A}\mathbf{D}(t)\right] \tag{A.47}$$

Where α is the inverse current variance and A is a diagonal matrix containing $\alpha = \{\alpha_n|n = 1 : N\}$. The current variance α^{-1} is assumed to be time-invariant. Whenever fMRI data is available, it may be used to provide an initial value to the currents' variance, otherwise setting the initial value for the current variance to be 1 for each dipole. After the first iteration, the inverse variance (precision) is estimated using an **Automatic Relevance Determination** (ARD) model[79] to place a hierarchical prior, which possesses a Gamma distribution $\Gamma\left(\alpha|\bar{\alpha},\gamma\right)$ with mean $\bar{\alpha}$ and shape parameter γ, as shown below:

$$\begin{aligned} P_0(\alpha) &= \prod_{n=1}^{N}\Gamma\left(\alpha_n|\bar{\alpha}_{0n}\ ,\gamma_{0n\alpha}\right) \\ \Gamma\left(\alpha|\bar{\alpha},\gamma\right) &\equiv \alpha^{-1}(\alpha\gamma/\bar{\alpha})\Gamma(\gamma)^{-1}e^{-\alpha\gamma/\bar{\alpha}} \end{aligned} \tag{A.48}$$

Where $\Gamma(\gamma) \equiv \int_0^\infty dt\ t^{\gamma-1}e^{-T}$ is the Gamma function and $\gamma_{0n\alpha}$ are hyperparameters directly controlling the width of the Gamma distribution. Whenever the mean value of the inverse current variance $\bar{\alpha}$ is small, it is more likely that the inverse current variance α will also have a small value, whereas whenever the mean is large, the probability of the inverse variance acquiring a large value increases. In the case when fMRI information is available, it can be used to initialize the values for the current variance. This results in regions with low inverse variance (so high variance) being assumed to be active. The current variance is then iteratively updated so that only dipoles depicting large variances remain.

Intermezzo: Automatic Relevance Determination (ARD) model

This description of the ARD model is based on the lecture by Florian Wilhelm[80] and the work of David MacKay[79].

The ARD model is meant to "prune" the amount of parameters used to fit a model to some data set by setting a threshold on the precision (inverse variance) of each of them and setting any parameter that crosses it to zero . It has been described already when discussing the regularization matrix Σ_0, which is why this intermezzo is only meant to underline the role it plays in the hVB method. Essentially, the ARD approach is used to estimate the hyperparameter α to achieve an adequately weighted solution for the L_2 regularization problem described earlier. The whole process consists on setting initial values for the hyperparameters, using them to evaluate some approximation of the desired quantity (i.e. Free Energy), updating the hyperparameters and comparing them to a threshold, and repeating until the solution converges. This process will be discussed in detail as the hVB method is described.

A.2.3 Smoothness constraint

In the original method described in Sato et al.[47], the smoothness constraint is applied to the off-diagonal terms of the covariance matrix. These terms are controlled by a second diagonal matrix dubbed Λ, which contains $\lambda = \{\lambda_n | n = 1 : N\}$ values that, the larger they are, the larger the correlation between each dipole and its corresponding neighbors is. These values are estimated using a hierarchical prior in the same way as for the inverse current variance, and are included in the current prior distribution as follows:

$$P_0(\mathbf{D}_{1:T}|\alpha, \lambda) \propto \exp\left[-\frac{1}{2}\sum_{t=1}^{T}\mathbf{D}'(t)\Sigma_\alpha\mathbf{D}(t)\right]$$
$$\Sigma_\alpha^{-1} = \mathbf{A}^{-1} + \mathbf{W}\Lambda^{-1}\mathbf{W}' \tag{A.49}$$

Where Σ_α^{-} 1 is the current covariance matrix and $\mathbf{W}$ is a Gaussian smoothing filter.

Equation A.34, which establishes the probability of the observed EEG signal given the current densities, may be rewritten to include the covariance matrix of the sensor noise, as:

$$P(\mathbf{M}|\mathbf{D},\beta) \propto \left[-\frac{1}{2}\beta(\mathbf{M}-\mathbf{GD})'\,\Sigma_G\,(\mathbf{M}-\mathbf{GD})\right] \tag{A.50}$$

Where β^{-1} is the average noise variance and $(\beta\Sigma_G)^{-1}$ is the full noise covariance matrix, estimated from the baseline of the EEG. Nevertheless, the VBMEG method may also apply a smoothness constraint based on the structural MRI data of each subject, in the form of a Gaussian smoothing filter, defined as:

$$(\mathbf{W}_L)_{nm} = \exp\left(-\left(d_{nm}/\sigma\right)^2\right) \tag{A.51}$$

In the Gaussian smoothing filter, d_{nm} is the shortest path between the nth and the mth vertices in the cortical model and σ is the standard deviation. A full width half maximum (FWHM) value of 8mm was assumed.

Intermezzo: Converting FWHM to the standard deviation σ

This brief explanation is based on[81].

The probability density function for a Gaussian distribution with mean μ and standard deviation σ is:

$$f(x) = \frac{1}{\sigma\sqrt{2\pi}}\exp\left(-\frac{(x-\mu)^2}{2\sigma^2}\right)$$

If this distribution is centered at the origin, the mean is zero and the FWHM is the distance from $-x_w$ to x_w , so $FWHM = x_w - (-x_w) = 2x_w$. To find the peak of the function, it is necessary to find the value of x_w that satisfies $f(x_w) = f(\mu)/2$. Substituting these values then yields:

$$\frac{1}{\sigma\sqrt{2\pi}}\exp\left(-\frac{x_w^2}{2\sigma^2}\right) = \frac{1}{2}\frac{1}{\sigma\sqrt{2\pi}}$$

$$x_w = \pm\sqrt{2\sigma^2\,ln2}$$

Therefore, the FWHM and the standard deviation are related as:

$$FWHM = \sigma\sqrt{8ln2}$$

This Gaussian filter is used on the Leadfield, as high correlations are assumed between neighboring dipoles. Under this assumption, the smoothed cortical currents **D** are defined as:

$$\mathbf{D}(t) = \mathbf{W}_L\mathbf{Z}(t) \tag{A.52}$$

This then calls for a re-definition of the quasi-static approximation for the scalp measurements shown in **equation 2.2** to be reformulated as:

$$\mathbf{M}(t) = \hat{\mathbf{G}}\mathbf{Z}(t) \tag{A.53}$$

Where $\hat{\mathbf{G}}$ is a smooth Leadfield matrix $\hat{\mathbf{G}} \equiv \mathbf{G}\mathbf{W}_L$ and $\mathbf{Z}(t)$ are the un-smoothed reconstructed currents.

With this smoothing constraint based on structural MRI, the current densities may be calculated as:

$$\begin{aligned} \mathbf{D}(t) &= \Sigma_\alpha^{-1}\,\mathbf{G}'(\mathbf{G}\,\Sigma_\alpha^{-1}\,\mathbf{G}' + \beta^{-1}\mathbf{I}_N)^{-1}\mathbf{M}(t) \\ \Sigma_{\alpha^{-1}} &= \mathbf{W}_L\,\mathbf{A}_L^{-1}\,\mathbf{W}_L' \end{aligned} \tag{A.54}$$

Where $\mathbf{A}_L^{-1} = diag(\alpha_L^{-1})$ is the variance matrix for **Z**.

Variational Bayesian Method

The problem to be solved was shown earlier in this appendix, in **equation A.26**. The idea is to use prior information on the distribution of the currents **D** to find their posterior distribution given a scalp potential **M**. The following equations were taken from the work of Sato et al.[47] in which the hVB method was introduced. The posterior distribution for the currents given the observed EEG signal is defined as:

$$P(\mathbf{D}|\mathbf{M}) = \int d\alpha\, P(\mathbf{D}, \alpha|\mathbf{M}) \tag{A.55}$$

The joint provability of the currents and the inverse current variance α given the measurements is:

$$
\begin{aligned}
P(\mathbf{D},\alpha|\mathbf{M}) &= \frac{P(\mathbf{D},\alpha,\mathbf{M})}{P(\mathbf{M})} \\
P(\mathbf{D},\alpha,\mathbf{M}) &= P(\mathbf{M}|\mathbf{D})P_0\left(\mathbf{D}|\alpha\right)P_0\left(\alpha\right) \\
P(\mathbf{M}) &= \int d\mathbf{D}d\alpha P(\mathbf{D},\alpha,\mathbf{M}) \qquad \text{(A.56)}
\end{aligned}
$$

The marginal likelihood (evidence) of the measured scalp potential cannot be calculated analytically, which is why the joint posterior distribution of the currents and their corresponding inverse variance given the measurements is reformulated as the maximization of the **Free Energy** (see *intermezzo* on Free Energy for a more detailed explanation on this subject). The *Free Energy* for a trial distribution $Q(\mathbf{D},\alpha)$ can be written as:

$$
\begin{aligned}
F(Q) &= \int d\mathbf{D}d\alpha Q(\mathbf{D},\alpha)log\left[\frac{P(\mathbf{D},\alpha,\mathbf{M})}{Q(\mathbf{D},\alpha)}\right] \\
&= \int d\mathbf{D}d\alpha Q(\mathbf{D},\alpha)log\left[\frac{P(\mathbf{M})P(\mathbf{D},\alpha|\mathbf{M})}{Q(\mathbf{D},\alpha)}\right] \qquad \text{(A.57)}
\end{aligned}
$$

This expression can be rearranged to fit the Kullback-Leibler Divergence (refer to *intermezzo* on this topic) to measure the difference between the trial distribution being tested and the joint posterior distribution $P(\mathbf{D},\alpha|\mathbf{M})$ and adopts the following form:

$$
\begin{aligned}
F(Q) &= log(P(\mathbf{M})) - \int d\mathbf{D}d\alpha Q(\mathbf{D},\alpha)log\left[\frac{Q(\mathbf{D},\alpha)}{P(\mathbf{D},\alpha|\mathbf{M})}\right] \\
&= log(P(\mathbf{M})) - KL[Q(D,\alpha)\|P(\mathbf{D},\alpha|\mathbf{M})] \qquad \text{(A.58)}
\end{aligned}
$$

As it may be noted, when both distributions are equal the whole KL term goes to zero, so the joint posterior $P(\mathbf{D},\alpha|\mathbf{M})$ may be obtained by maximizing the *Free Energy* with respect to the trial distribution Q and the log-marginal likelihood log(P($\mathbf{M}$)) equals the *Free Energy*.

Intermezzo: Kullback-Leibler Divergence

This brief explanation was taken from[82][83].

The Kullback-Leibler Divergence is used as an indicator of the difference between two probability distributions over the same variable. If, for example, a comparison is to be made between the "true" distribution $p(x)$ and a trial distribution $q(x)$, defined in an attempt to describe $p(x)$, the Kullback-Leibler divergence from $p(x)$ to $q(x)$ is defined as:

$$KL[q(x)\|p(x)] = \int_{-\infty}^{\infty} q(x) log \frac{q(x)}{p(x)} dx \tag{A.59}$$

By this definition, when the the trial distribution is equal to the true distribution, the KL distance goes to zero.

Intermezzo: Free Energy Principle

The following explanation is based on the work of Karl Friston[84][85].

The Free Energy principle enounces that any self-organizing system in homeostatic equilibrium must minimize its free energy. To maintain this equilibrium, the system has a set of states identified to be acceptable for preserving its stability, called a global random attractor, each of which states must have a low entropy (also called "surprise") or lack of predictability. The system cannot avoid "surprises", but the free energy constitutes an upper bound for surprise. This means that minimizing the free energy minimizes surprise as well. The free energy depends on two aspects, the sensory states of the system and a recognition density encoded by its internal states. A recognition density is an approximate probability distribution of the causes of data (i.e. sensory input). The Free Energy is defined as:

$$\begin{aligned} F(x(t)) &= L(s(t)) + \int_{\Psi} q(\psi(t)|\mu(t))\, ln \frac{q(\psi(t)|\mu(t))}{p(\psi(t))|s(t), m)} d\psi \\ &= L(s(t)) + KL[q(\psi(t)|\mu(t))\|p(\psi(t))|s(t), m)] \end{aligned}$$

Where $\psi(t) \in \Psi$ is a set of unobservable fictive random variables (they only exist to parametrize the marginal likelihood), $\mu(t)$ are internal states, m is a probabilistic generative model and s(t) are sensory signals. L(s(t)) is the self-information or *surprisal*, and is equal to:

$$L(s(t)) = -ln(p(s(t)|m))$$

$p(s|m)$ is the ergodic density and it is an invariant probability measure of finding the system in any state when observed at a random point in time. When the KL divergence is zero, the Free Energy approximates the ergodicity perfectly (exact Bayesian inference), but when the form of the proposed model does not match the conditional density, only an approximate Bayesian inference is achieved.

The present work is based on the so-called *Bayesian Brain Hypothesis*, which says the brain has a model of the world being constantly optimized using sensory inputs, making inferences about the causes for such inputs.

Based on the explanation provided in the *Free Energy Intermezzo* and the factorization assumption $Q(D,\alpha) = Q_D(D)Q_\alpha(\alpha)$[68], the free energy may be expressed as:

$$\begin{aligned} F(Q) &= \langle logP(\mathbf{D},\alpha,\mathbf{M})\rangle_\alpha - \langle logQ_D(D)\rangle_D - \langle logQ_\alpha(\alpha)\rangle_\alpha \\ &= \langle log(M|D)\rangle_D - KL[Q_D(D)Q_\alpha(\alpha)\|P_0(D|\alpha)P_0(\alpha)] \end{aligned} \qquad (A.60)$$

Where $\langle\rangle_D$ and $\langle\rangle_\alpha$ represent the expectation value with respect to $Q_D(D)$ and $Q_\alpha(\alpha)$, respectively. The maximum free energy is calculated by alternatively maximizing the Free Energy with respect to Q_D and Q_α until the Free Energy converges. The first step, denominated *D-step* here, consists on a maximization with respect to Q_D while Q_α is fixed.

$$Q_D(D) \propto \exp\left[\langle logP(\mathbf{D},\alpha,\mathbf{M})\rangle_\alpha\right] \qquad (A.61)$$

In the second step, here called the *α-step*, the Free Energy is maximized with respect to Q_α while Q_D is fixed.

$$Q_\alpha(\alpha) \propto \exp\left[\langle logP(\mathbf{D},\alpha,\mathbf{M})\rangle_D\right] \qquad (A.62)$$

hVB Algorithm

The steps of the hVB algorithm are summarized in **table A.1**, where Σ_α^{-1} is the estimated covariance matrix and $\Sigma_B = \mathbf{G}\Sigma_\alpha^{-1}\mathbf{G}' + \Sigma_G^{-1}$. Σ_C is a diagonal matrix with the Trace of the Autocovariance matrix C_{uu} repeated along its diagonal.

A.2.4 Tools used in NETMAR

Singular Value Decomposition (SVD)

The following explanation is based on the overview from Jepson and Flores-Mangas[86] and this Wikipedia article[87].

The SVD is the factorization of a matrix into an orthonormal rotation matrix $\mathbf{V}^T$, a scaling diagonal matrix Σ with the so-called singular values on its diagonal (non-negative, listed from largest to smallest) and another rotation matrix $\mathbf{U}$, with respect to the coordinate axes.

In the present work, the solution to the least-squares problem would be given by:

Table A.1: hVB Static Estimation

Step	Task	Equation
Noise Covariance	Definition	$\Sigma_G^{-1} = C_{uu} + \Sigma_C$
D-step	Inverse Filter	$\mathbf{L}(\Sigma_\alpha^{-1}) = \Sigma_\alpha^{-1}\,\mathbf{G}'\,\Sigma_B^{-1}$
D-step	Estimate Current	$\mathbf{Z}(t) = \mathbf{L}(\Sigma_\alpha^{-1})\,\mathbf{M}(t)$
α-step	Estimate Variance	$\alpha_n^{-1} = \frac{\gamma_{0n\alpha}\bar{\alpha}_{0n}^{-1} + \frac{T}{2}\left(\frac{1}{T}\sum_{t=1}^{T}\mathbf{D}_n^2(t)\right)}{\gamma_{0n\alpha} + \frac{T}{2}(\mathbf{L}(\Sigma_\alpha^{-1})\ \mathbf{G})_{n,n}}$
α-step	Estimate Covariance	$\Sigma_\alpha^{-1} = diag(\alpha_n^{-1})$
Inverse Filter	-	$\mathbf{L}(\Sigma_\alpha^{-1}) = \Sigma_\alpha^{-1}\,\mathbf{G}'\,\Sigma_B^{-1}$
Current reconstruction	-	$\mathbf{Z}(t) = \mathbf{L}(\Sigma_\alpha^{-1})\mathbf{M}(t)$
Current smoothing	Apply Gaussian filter	$\mathbf{D}(\mathrm{t})=\mathbf{W}\mathbf{Z}(\mathrm{t})$

$$\mathbf{A}_l = \mathbf{V}(\mathbf{R}(\mathbf{U}^T\mathbf{D}_t))$$

Where **R** is the pseudoinverse of the diagonal matrix Σ.

There are many applications for the SVD, such as the calculation of the pseudo-inverse of a matrix, the solution of homogeneous linear equations and the solution of the total least-squares minimization.

Appendix B

EEG Preprocessing: Bad component rejection

The rejection for bad components present in the ERP extracted from the EEG signal is not always straightforward and it requires practice. This appendix is dedicated to providing examples of artefactual components and highlights which aspects to take into account for cleaning the signal.

Section 3.2.3 outlines the steps followed to preprocess the EEG signal in the present work. After running ICA, the first step towards rejecting artefactual components is to plot the properties of each component. This was done in EEGlab using Plot-Component Properties. An example of a "good" component is shown in **Figure B.1**.

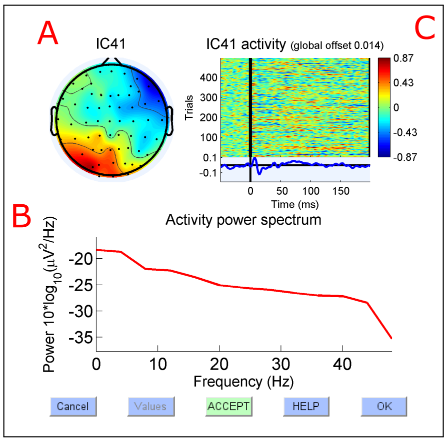

Figure B.1: Example of a good independent component, found using ICA

The first aspect to which attention must be paid is the topographical representation of the component (A in **Figure B.1**). A good independent component depicts a spread activity over multiple electrodes. The second aspect is the activity power spectrum (B), which must be monotonically decreasing. Different degrees of steepness may be observed, but sudden decays may reflect visual artifacts, like the one shown in **Figure B.2**. The third aspect to take into account is the activity over time (C). The averaged signal over trials must not show activity before the stimulus onset, as doing so may confirm the component as an artifact. **Figure B.3** shows examples of components corresponding to muscle artifacts.

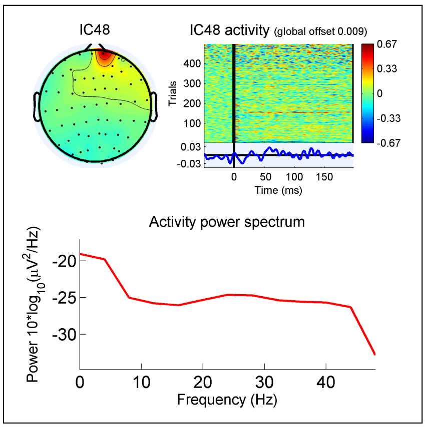

Figure B.2: Example of a visual artifact independent component, found using ICA. Notice the sudden drop in the power spectrum, as well as the activity before stimulus onset

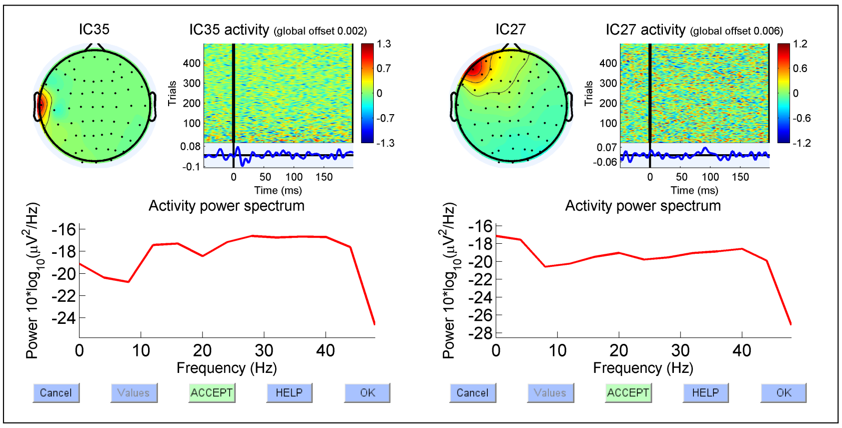

Figure B.3: Example of muscle artifacts independent components, found using ICA. Besides the concentration at a single electrode, the power spectrum does not decrease gradually

Bad components like the ones shown in **Figure B.2** and **B.3** must be removed manually using the component rejection tool from EEGlab.

Bibliography

[1] WHO, "Stroke, cerebrovascular accident." `http://www.who.int/topics/cerebrovascular_accident/en/`. (Accessed on 02/13/2017).

[2] S. Standring and N. Borley, *Gray's Anatomy: The Anatomical Basis of Clinical Practice.* ClinicalKey 2012, Churchill Livingstone/Elsevier, 2008.

[3] WHO, "Cardiovascular diseases." `http://www.who.int/cardiovascular_diseases/en/cvd_atlas_01_types.pdf?ua=1`. (Accessed on 02/13/2017).

[4] ESO, "Stroke resources - european stroke organisation." `http://eso-stroke.org/stroke-resources/`. (Accessed on 02/11/2017).

[5] A. S. Association, "Understanding stroke risk." `http://www.strokeassociation.org/STROKEORG/AboutStroke/UnderstandingRisk/Understanding-Stroke-Risk_UCM_308539_SubHomePage.jsp`. (Accessed on 03/21/2017).

[6] T. Truelsen, B. Piechowski-Jóźwiak, R. Bonita, C. Mathers, J. Bogousslavsky, and G. Boysen, "Stroke incidence and prevalence in europe: a review of available data," *European journal of neurology*, vol. 13, no. 6, pp. 581–598, 2006.

[7] A. S. Go, D. Mozaffarian, V. L. Roger, E. J. Benjamin, J. D. Berry, M. J. Blaha, S. Dai, E. S. Ford, C. S. Fox, S. Franco, *et al.*, "Heart disease and stroke statistics-2014 update," *Circulation*, vol. 129, no. 3, 2014.

[8] WHO, "Burden of stroke." `http://www.who.int/cardiovascular_diseases/en/cvd_atlas_15_burden_stroke.pdf?ua=1`. (Accessed on 02/13/2017).

[9] A. H. Association *et al.*, "Heart disease and stroke statistics at a glance. 2015," 2016.

[10] CVD, "cvd_atlas_17_economics.pdf." `http://www.who.int/cardiovascular_diseases/en/cvd_atlas_17_economics.pdf?ua=1`. (Accessed on 02/13/2017).

[11] RIVM, "The disease impact, health care management, and costs of stroke in the netherlands." `http://rivm.nl/bibliotheek/rapporten/282701001.pdf`. (Accessed on 02/13/2017).

[12] J. N. Struijs, M. L. van Genugten, S. M. Evers, A. J. Ament, C. A. Baan, and G. A. van den Bos, "Modeling the future burden of stroke in the netherlands," *Stroke*, vol. 36, no. 8, pp. 1648–1655, 2005.

[13] C. D. Wolfe, "The impact of stroke," *British medical bulletin*, vol. 56, no. 2, pp. 275–286, 2000.

[14] M. van Eeden, C. M. van Heugten, and S. M. Evers, "The economic impact of stroke in the netherlands: the euro restore4stroke study," *BMC Public Health*, vol. 12, no. 1, p. 122, 2012.

[15] M. Van Eeden, C. van Heugten, G. van Mastrigt, M. van Mierlo, J. Visser Meily, and S. Evers, "The burden of stroke in the netherlands: estimating quality of life and costs for 1 year poststroke," *BMJ open*, vol. 5, no. 11, p. e008220, 2015.

[16] C. Winters, E. E. van Wegen, A. Daffertshofer, and G. Kwakkel, "Generalizability of the proportional recovery model for the upper extremity after an ischemic stroke," *Neurorehabilitation and neural repair*, vol. 29, no. 7, pp. 614–622, 2015.

[17] E. Wressle, B. Oberg, and C. Henriksson, "The rehabilitation process for the geriatric stroke patient-an exploratory study of goal setting and interventions," *Disability and rehabilitation*, vol. 21, no. 2, pp. 80–87, 1999.

[18] G. Nelles, G. Spiekermann, M. Jueptner, G. Leonhardt, S. Müller, H. Gerhard, and H. C. Diener, "Reorganization of sensory and motor systems in hemiplegic stroke patients," *Stroke*, vol. 30, no. 8, pp. 1510–1516, 1999.

[19] N. Byl, J. Roderick, O. Mohamed, M. Hanny, J. Kotler, A. Smith, M. Tang, and G. Abrams, "Effectiveness of sensory and motor rehabilitation of the upper limb following the principles of neuroplasticity: patients stable poststroke," *Neurorehabilitation and neural repair*, vol. 17, no. 3, pp. 176–191, 2003.

[20] P. Langhorne, F. Coupar, and A. Pollock, "Motor recovery after stroke: a systematic review," *The Lancet Neurology*, vol. 8, no. 8, pp. 741–754, 2009.

[21] K. N. Arya, S. Pandian, R. Verma, and R. Garg, "Movement therapy induced neural reorganization and motor recovery in stroke: a review," *Journal of bodywork and movement therapies*, vol. 15, no. 4, pp. 528–537, 2011.

[22] "Long-term potentiation - wikipedia." `https://en.wikipedia.org/wiki/Long-term_potentiation`. (Accessed on 03/13/2017).

[23] "Long-term depression - wikipedia." `https://en.wikipedia.org/wiki/Long-term_depression`. (Accessed on 03/13/2017).

[24] B. B. Johansson, "Brain plasticity and stroke rehabilitation," *Stroke*, vol. 31, no. 1, pp. 223–230, 2000.

[25] J. B. Green, "Brain reorganization after stroke," *Topics in stroke rehabilitation*, vol. 10, no. 3, pp. 1–20, 2003.

[26] A. K. Rehme and C. Grefkes, "Cerebral network disorders after stroke: evidence from imaging-based connectivity analyses of active and resting brain states in humans," *The Journal of physiology*, vol. 591, no. 1, pp. 17–31, 2013.

[27] O. Sporns, G. Tononi, and R. Kötter, "The human connectome: a structural description of the human brain," *PLoS Comput Biol*, vol. 1, no. 4, p. e42, 2005.

[28] G. Silasi and T. H. Murphy, "Stroke and the connectome: how connectivity guides therapeutic intervention," *Neuron*, vol. 83, no. 6, pp. 1354–1368, 2014.

[29] S. Baillet, J. C. Mosher, and R. M. Leahy, "Electromagnetic brain mapping," *IEEE Signal processing magazine*, vol. 18, no. 6, pp. 14–30, 2001.

[30] R. Hyder, N. Kamel, T. B. Tang, *et al.*, "Brain source localization techniques: Evaluation study using simulated eeg data," in *Biomedical Engineering and Sciences (IECBES), 2014 IEEE Conference on*, pp. 942–947, IEEE, 2014.

[31] M. Fukushima, O. Yamashita, T. R. Knösche, and M.-a. Sato, "Meg source reconstruction based on identification of directed source interactions on whole-brain anatomical networks," *NeuroImage*, vol. 105, pp. 408–427, 2015.

[32] A. Crouzeix, B. Yvert, O. Bertrand, and J. Pernier, "An evaluation of dipole reconstruction accuracy with spherical and realistic head models in meg," *Clinical Neurophysiology*, vol. 110, no. 12, pp. 2176–2188, 1999.

[33] A. Solodkin, U. Hasson, R. Siugzdaite, M. Schiel, E. E. Chen, K. Rolf, and S. L. Small, "Virtual brain transplantation (vbt): a method for accurate image registration and parcellation in large cortical stroke," *Archives italiennes de biologie*, vol. 148, no. 3, pp. 219–241, 2010.

[34] J. C. Mosher, R. M. Leahy, and P. S. Lewis, "Eeg and meg: forward solutions for inverse methods," *IEEE Transactions on Biomedical Engineering*, vol. 46, no. 3, pp. 245–259, 1999.

[35] "Boundaryelementmethod.pdf." `https://web.stanford.edu/class/energy281/BoundaryElementMethod.pdf`. (Accessed on 03/13/2017).

[36] R. D. Pascual-Marqui, "Review of methods for solving the eeg inverse problem," *International journal of bioelectromagnetism*, vol. 1, no. 1, pp. 75–86, 1999.

[37] R. Grech, T. Cassar, J. Muscat, K. P. Camilleri, S. G. Fabri, M. Zervakis, P. Xanthopoulos, V. Sakkalis, and B. Vanrumste, "Review on solving the inverse problem in eeg source analysis," *Journal of neuroengineering and rehabilitation*, vol. 5, no. 1, p. 25, 2008.

[38] L. Harrison, W. D. Penny, and K. Friston, "Multivariate autoregressive modeling of fmri time series," *Neuroimage*, vol. 19, no. 4, pp. 1477–1491, 2003.

[39] D. W. Shattuck and R. M. Leahy, "Brainsuite: an automated cortical surface identification tool," *Medical image analysis*, vol. 6, no. 2, pp. 129–142, 2002.

[40] Freesurfer, "recon all free surfer wiki." `https://surfer.nmr.mgh.harvard.edu/fswiki/recon-all`. (Accessed on 02/10/2017).

[41] SPM, "Microsoft word - spm8 processing steps.doc." `http://ccpweb.wustl.edu/pdfs/spm8processingman.pdf`. (Accessed on 02/10/2017).

[42] Mathworks, "Fill gaps using autoregressive modeling - matlab fillgaps." `https://www.mathworks.com/help/signal/ref/fillgaps.html`. (Accessed on 02/10/2017).

[43] MathWorks, "Reduce number of patch faces - matlab reducepatch." `https://www.mathworks.com/help/matlab/ref/reducepatch.html`. (Accessed on 05/09/2017).

[44] J. L. R. Andersson and S. N. Sotiropoulos, "An integrated approach to correction for off-resonance effects and subject movement in diffusion mr imaging." `https://fsl.fmrib.ox.ac.uk/fsl/fslwiki/eddy`. (Accessed on 05/09/2017).

[45] A. JLR, J. M, and S. S, "Non-linear registration, aka spatial normalisation." `https://fsl.fmrib.ox.ac.uk/fsl/fslwiki/FNIRT`, 2010. (Accessed on 05/09/2017).

[46] "Mrtrix3." `http://www.mrtrix.org/`. (Accessed on 05/09/2017).

[47] M.-a. Sato, T. Yoshioka, S. Kajihara, K. Toyama, N. Goda, K. Doya, and M. Kawato, "Hierarchical bayesian estimation for meg inverse problem," *NeuroImage*, vol. 23, no. 3, pp. 806–826, 2004.

[48] O. Yamashita, A. Galka, T. Ozaki, R. Biscay, and P. Valdes-Sosa, "Recursive penalized least squares solution for dynamical inverse problems of eeg generation," *Human brain mapping*, vol. 21, no. 4, pp. 221–235, 2004.

[49] J. Brownlee, "How to model residual errors to correct time series forecasts with python - machine learning mastery." `http://machinelearningmastery.com/model-residual-errors-correct-time-series-forecasts-python/`, January 2017. (Accessed on 05/09/2017).

[50] H. Hämäläinen, J. Kekoni, M. Sams, K. Reinikainen, and R. Näätänen, "Human somatosensory evoked potentials to mechanical pulses and vibration: contributions of si and sii somatosensory cortices to p50 and p100 components," *Electroencephalography and clinical neurophysiology*, vol. 75, no. 1, pp. 13–21, 1990.

[51] R. D. Pascual-Marqui *et al.*, "Standardized low-resolution brain electromagnetic tomography (sloreta): technical details," *Methods Find Exp Clin Pharmacol*, vol. 24, no. Suppl D, pp. 5–12, 2002.

[52] T. Yoshioka, K. Toyama, M. Kawato, O. Yamashita, S. Nishina, N. Yamagishi, and M.-a. Sato, "Evaluation of hierarchical bayesian method through retinotopic brain activities reconstruction from fmri and meg signals," *Neuroimage*, vol. 42, no. 4, pp. 1397–1413, 2008.

[53] "Signal-to-noise ratio - wikipedia." `https://en.wikipedia.org/wiki/Signal-to-noise_ratio`. (Accessed on 05/16/2017).

[54] Wikipedia, "Signal-to-noise ratio." `https://en.wikipedia.org/wiki/Signal-to-noise_ratio`. (Accessed on 06/02/2017).

[55] M. E. Newman, "Modularity and community structure in networks," *Proceedings of the national academy of sciences*, vol. 103, no. 23, pp. 8577–8582, 2006.

[56] F. Babiloni, C. Babiloni, F. Carducci, G. L. Romani, P. M. Rossini, L. M. Angelone, and F. Cincotti, "Multimodal integration of eeg and meg data: A simulation study with variable signal-to-noise ratio and number of sensors," *Human brain mapping*, vol. 22, no. 1, pp. 52–62, 2004.

[57] S. Luck, "Ten simple rules for designing and interpreting erp experiments.[in:] event-related potentials: A methods handbook," *Handy, TC (Ed.)*, 2004.

[58] N. A. Parks, M. A. Gannon, S. M. Long, and M. E. Young, "Bootstrap signal-to-noise confidence intervals: an objective method for subject exclusion and quality control in erp studies," *Frontiers in human neuroscience*, vol. 10, 2016.

[59] A. K. Rehme, S. B. Eickhoff, C. Rottschy, G. R. Fink, and C. Grefkes, "Activation likelihood estimation meta-analysis of motor-related neural activity after stroke," *Neuroimage*, vol. 59, no. 3, pp. 2771–2782, 2012.

[60] K. Takeda, Y. Gomi, and H. Kato, "Near-infrared spectroscopy and motor lateralization after stroke: a case series study," *Int. J. Phys. Med. Rehabil*, vol. 2, p. 192, 2014.

[61] T. R. Knösche, A. Anwander, M. Liptrot, and T. B. Dyrby, "Validation of tractography: Comparison with manganese tracing," *Human brain mapping*, vol. 36, no. 10, pp. 4116–4134, 2015.

[62] C. Bordier, C. Nicolini, and A. Bifone, "Graph analysis and modularity of brain functional connectivity networks: searching for the optimal threshold," *arXiv preprint arXiv:1705.06481*, 2017.

[63] A. R. Carter, G. L. Shulman, and M. Corbetta, "Why use a connectivity-based approach to study stroke and recovery of function?," *Neuroimage*, vol. 62, no. 4, pp. 2271–2280, 2012.

[64] D. Meunier, S. Achard, A. Morcom, and E. Bullmore, "Age-related changes in modular organization of human brain functional networks," *Neuroimage*, vol. 44, no. 3, pp. 715–723, 2009.

[65] S. Rusinkiewicz and M. Levoy, "Efficient variants of the icp algorithm," in *3-D Digital Imaging and Modeling, 2001. Proceedings. Third International Conference on*, pp. 145–152, IEEE, 2001.

[66] H. Liu, P. H. Schimpf, G. Dong, X. Gao, F. Yang, and S. Gao, "Standardized shrinking loreta-focuss (sslofo): a new algorithm for spatio-temporal eeg source reconstruction," *IEEE Transactions on Biomedical Engineering*, vol. 52, no. 10, pp. 1681–1691, 2005.

[67] C. Silva, J. Maltez, E. Trindade, A. Arriaga, and E. Ducla-Soares, "Evaluation of l1 and l2 minimum norm performances on eeg localizations," *Clinical neurophysiology*, vol. 115, no. 7, pp. 1657–1668, 2004.

[68] M.-A. Sato, "Online model selection based on the variational bayes," *Neural Computation*, vol. 13, no. 7, pp. 1649–1681, 2001.

[69] Y. Yang, T. Solis-Escalante, M. van de Ruit, F. C. van der Helm, and A. C. Schouten, "Nonlinear coupling between cortical oscillations and muscle activity during isotonic wrist flexion," *Frontiers in Computational Neuroscience*, vol. 10, 2016.

[70] "4d-eeg: Home." `http://www.4deeg.eu/`. (Accessed on 05/25/2017).

[71] T. Sato, I. Nambu, K. Takeda, T. Aihara, O. Yamashita, Y. Isogaya, Y. Inoue, Y. Otaka, Y. Wada, M. Kawato, *et al.*, "Reduction of global interference of scalp-hemodynamics in functional near-infrared spectroscopy using short distance probes," *NeuroImage*, vol. 141, pp. 120–132, 2016.

[72] N. Instruments, “Selecting a model structure in the system identification process.” `http://www.ni.com/white-paper/4028/en/`, June 2010. (Accessed on 05/22/2017).

[73] N. S. Ward, “Does neuroimaging help to deliver better recovery of movement after stroke?,” *Current opinion in neurology*, vol. 28, no. 4, pp. 323–329, 2015.

[74] M. Hamalainen, R. Hari, R. J. Ilmoniemi, J. Knuutila, and O. V. Lounasmaa, “Magnetoencephalography theory, instrumentation, and applications to noninvasive studies of the working human brain,” *Reviews of modern Physics*, vol. 65, no. 2, p. 413, 1993.

[75] “390_pf_07.dvi.” `http://www.ezra.chem.cornell.edu/390_pf_07.pdf`. (Accessed on 03/15/2017).

[76] “Calculating probability and the partition function.” `http://www.isn-oldenburg.de/~hilf/vortraege/twente99/stat12/node3.html`. (Accessed on 03/15/2017).

[77] A. J. Laub, *Matrix Analysis for Scientists and Engineers.* SIAM, 2005.

[78] “The laplace operator.” `http://fourier.eng.hmc.edu/e161/lectures/gradient/node7.html`. (Accessed on 03/18/2017).

[79] D. J. MacKay *et al.*, “Bayesian nonlinear modeling for the prediction competition,” *ASHRAE transactions*, vol. 100, no. 2, pp. 1053–1062, 1994.

[80] F. Wilhelm, “The idea behind automatic relevance determination and bayesian interpolation - youtube.” `https://www.youtube.com/watch?v=2gT-Q0NZzoE`, March 2016. (Accessed on 04/10/2017).

[81] “Gaussian kernels: convert fwhm to sigma | brainder..” `https://brainder.org/2011/08/20/gaussian-kernels-convert-fwhm-to-sigma/`. (Accessed on 04/05/2017).

[82] “Kl-divergence.pdf.” `http://web.engr.illinois.edu/~hanj/cs412/bk3/KL-divergence.pdf`. (Accessed on 04/08/2017).

[83] “Kullback - leibler divergence - wikipedia.” `https://en.wikipedia.org/wiki/Kullback%E2%80%93Leibler_divergence`. (Accessed on 04/08/2017).

[84] K. Friston, “The free-energy principle: a unified brain theory?,” *Nature Reviews Neuroscience*, vol. 11, no. 2, pp. 127–138, 2010.

[85] F. Karl, “A free energy principle for biological systems,” *Entropy*, vol. 14, no. 11, pp. 2100–2121, 2012.

[86] A. Jepson and F. Flores Mangas, “The singular value decomposition.” `http://www.cs.toronto.edu/~jepson/csc420/notes/introSVD.pdf`, September 2011. (Accessed on 04/22/2017).

[87] “Singular value decomposition - wikipedia.” `https://en.wikipedia.org/wiki/Singular_value_decomposition`. (Accessed on 04/22/2017).

[88] J. J. Dziak, D. L. Coffman, S. T. Lanza, and R. Li, “Sensitivity and specificity of information criteria,” *The Methodology Center and Department of Statistics, Penn State, The Pennsylvania State University*, pp. 1–10, 2012.

List of Figures

List of Tables